

Alma Mater Studiorum Università di Bologna
Archivio istituzionale della ricerca

Fluid-mediated selective dissolution of subducting carbonaceous material: Implications for carbon recycling and fluid fluxes at forearc depths

This is the final peer-reviewed author's accepted manuscript (postprint) of the following publication:

Published Version:

Vitale Brovarone A., Tumiatì S., Piccoli F., Ague J.J., Connolly J.A.D., Beyssac O. (2020). Fluid-mediated selective dissolution of subducting carbonaceous material: Implications for carbon recycling and fluid fluxes at forearc depths. *CHEMICAL GEOLOGY*, 549, 1-19 [10.1016/j.chemgeo.2020.119682].

Availability:

This version is available at: <https://hdl.handle.net/11585/827256> since: 2024-05-03

Published:

DOI: <http://doi.org/10.1016/j.chemgeo.2020.119682>

Terms of use:

Some rights reserved. The terms and conditions for the reuse of this version of the manuscript are specified in the publishing policy. For all terms of use and more information see the publisher's website.

This item was downloaded from IRIS Università di Bologna (<https://cris.unibo.it/>).
When citing, please refer to the published version.

(Article begins on next page)

Fluid-mediated selective dissolution of subducting carbonaceous material: implications for carbon recycling and fluid fluxes at forearc depths

Alberto VITALE BROVARONE^{1,2*}, Simone TUMIATI³, Francesca PICCOLI⁴, Jay J. AGUE^{5,6}, James A. CONNOLLY⁷, Olivier BEYSSAC¹

¹ Institut de Minéralogie, de Physique des Matériaux et de Cosmochimie (IMPMC), Sorbonne Université, Muséum National d'Histoire Naturelle, UMR CNRS 7590, IRD UR206, 75005 Paris, France

² Dipartimento di Scienze della Terra, Università degli Studi di Torino, Via Valperga Caluso 35, 10125 Torino, Italy

³ Dipartimento di Scienze della Terra, Università degli Studi di Milano, via Mangiagalli 34, 20133 Milano, Italy

⁴ Institute of Geological Sciences, University of Bern, 3012 Bern, Switzerland

⁵ Department of Geology and Geophysics, Yale University, New Haven, CT 06520, USA

⁶ Yale Peabody Museum of Natural History, New Haven, CT 06520, USA

⁷ Department of Earth Science, Swiss Federal Institute of Technology, Zurich, Switzerland

* Corresponding author: alberto.vitale@unito.it

Abstract

Subduction of crustal C governs the long-term global C cycling. The role of carbonates recycling in subduction zones and the related dissolution of C at various depths have been the subject of a large body of literature over the last decades. Much less is known about the contribution of carbonaceous material (CM) to the deep C cycling in subduction zones. This paper presents natural evidence for intense fluid-mediated leaching of CM in pelitic schists at high-pressure/low-temperature conditions relevant to the forearc region of subducting slabs. Manifestations of such process were identified along fluid pathways at various scales in the blueschist-facies subduction complexes of both Alpine Corsica and the Western Alps. Microstructural, whole-rock and Raman analyses across a selected metasomatic aureole were used to quantify the amount and mechanisms of C loss during fluid-rock interaction. In samples affected by intense fluid infiltration, more than 90% of the initial CM was removed from the rock. Microstructural and micro-Raman data indicate selective leaching of disordered CM relative to nearly crystalline graphite. The collected data allowed constraining the magnitude of fluid fluxes required to bleach the studied CM-bearing lithologies at different P-T-fO₂ conditions, which corresponds to rather high time-integrated fluid fluxes in the order of $\sim 10^6$ m³/m². In settings of large-scale fluid channelization, such as along regional-scale, lithological/tectonic boundaries or at the top of the subducted sedimentary pile, intense dissolution of subducted CM is expected. This process may thus exert a negative feedback on the sink of C phases into the deep mantle over the geological timescales and contribute to the release of isotopically light C from subducting slabs in forearc regions.

1. Introduction

Subduction of crustal C plays a central role in the global C cycle. Carbonate mineral and carbonaceous material (CM) are the main reservoirs of C in subducting slabs (Hayes and Waldbauer, 2006; Plank, 2014). Metamorphism of carbonate minerals, through either decarbonation/melting reactions or dissolution, has been the focus of considerable research over the last decades (Ague and Nicolescu, 2014; Cook-Kollars et al., 2014; Facq et al., 2014; Gorman et al., 2006; Kelemen and Manning, 2015; Poli, 2015). The contribution of carbonaceous material (CM) to deep C fluxes is less well known, despite the fact that CM is the main input of organic C to subduction zones (Hayes and Waldbauer, 2006; Plank, 2014). With rising temperature during subduction, CM is progressively transformed into graphite through a series of intermediate stages of disordered graphitic C (Buseck and Beyssac, 2014). The progressive transformation of CM into graphite results in loss of heteroatoms such as O, H, and N, as well as some C. Release of C during the earliest transformations of subducted carbonaceous material ($< 300\text{ }^{\circ}\text{C}$) is well established and results in the release of C compounds including thermogenic hydrocarbons and CO_2 (Mullis et al., 1994; Tarantola et al., 2007). At higher metamorphic grades, the behavior of CM is generally considered less mobile than carbonate minerals. Owing to its high buffering potential in oxidized geological fluids (Duncan and Dasgupta, 2017; Hermann et al., 2006), graphitic C, especially crystalline graphite, may be largely retained in the rock even at high temperature conditions. For example, CM is dominantly retained in sedimentary rocks heated by contact metamorphism to temperatures of $600\text{ }^{\circ}\text{C}$ or more (Pattison, 2006). At similar temperature but higher pressure conditions, dissolution of CM is documented during regional Barrovian-style metamorphism of the Wepawaug Schist, Connecticut, USA (Zhang et al., 2018). In this case, a loss of about 26% of the bulk rock CM content was observed in kyanite-bearing metapelites ($\sim 600^{\circ}\text{C}$) with respect to lower-grade chlorite-biotite zone precursors. In subduction zones, analysis of sedimentary rocks metamorphosed under closed system conditions suggests that more than 75% of the initial subducted CM is preserved down to depths of $\sim 100\text{ km}$ (Cook-Kollars et al., 2014).

However, the behavior of subducted CM in open system conditions, e.g. along fluid percolation pathways, is less constrained. Most studies focusing on the behavior of reduced C in open systems have dealt with graphite deposition (Duke and Rumble, 1986; Evans et al., 2002; Galvez et al., 2013; Luque et al., 2009; Vitale Brovarone et al., 2017), whereas fluid-mediated removal of CM is still scarcely documented (Mori et al., 2014). In particular, fluid-rock interactions along channelized fluid pathways may strongly affect the stability of C-bearing phases, as shown for carbonate minerals through processes of decarbonation (Gorman et al., 2006), fluid-mediated carbonate dissolution (Ague and Nicolescu, 2014), or carbonation (Piccoli et al., 2016). Under these circumstances, the conditions suitable for CM mobilization

(Tumiati and Malaspina, 2019; Tumiati et al., 2017) may be enhanced relative to closed systems. In particular, although the solubility of CM may be low in aqueous fluids, protracted and/or repeated infiltration of aqueous fluids into CM-bearing lithologies has the potential to progressively remove organic C from the rock.

In this contribution, we document natural evidence for fluid-mediated dissolution of CM in metasedimentary rocks at blueschist-facies, high-pressure/low-temperature (HP/LT) conditions within the Schistes Lustrés complex of Alpine Corsica and Western Alps. After a general presentation of the characteristic rocks and microstructures, detailed mineralogical and geochemical data is presented for a selected metasomatic aureole from Alpine Corsica. Microstructural data, bulk CM concentrations, Raman spectroscopy, and thermodynamic calculations are integrated to describe the patterns of fluid rock interactions and dissolution of CM, to estimate the time-integrated fluid fluxes along channelized fluid pathways in the subducting slab at forearc depths, and to examine the related geochemical implications.

2. Geologic setting

The Schistes Lustrés complex of Alpine Corsica and Western Alps (Fig. 1) mainly consists of Tethyan oceanic/transitional metaophiolitic rocks and associated metasedimentary cover rocks units that were variably transformed in the Alpine subduction system (Agard et al., 2001; 2002; Beltrando et al., 2010; Elter, 1971; Lagabriele et al., 2015). In both belts, these units underwent high-pressure/low-temperature (HP/LT) metamorphism ranging from low-grade to lawsonite eclogite-facies conditions (Agard et al., 2009; Angiboust et al., 2009; Fournier et al., 1991; Groppo and Castelli, 2010; Ravna et al., 2010; Schwartz et al., 2013; Vitale Brovarone et al., 2013).

This study centers on the blueschist-facies domain of the Schistes Lustrés complex exposed in Alpine Corsica and Western Alps (Fig. 1). In both belts, this terrane consists mostly of large metasedimentary suites containing variable proportions of CM-rich metapelitic schists and marble layers that incorporate blocks and slices of mafic and ultramafic rocks such as metagabbros, metabasalts, and serpentinites. The juxtaposition of mafic/ultramafic and oceanic sedimentary lithologies are interpreted as the result of pre-subduction gravitational and/or tectonic lithological associations only locally intensely reworked by the Alpine tectonics (Balestro et al., 2015; Lagabriele et al., 2015; Lagabriele and Lemoine, 1997; Lemoine, 2003; Polino and Lemoine, 1984; Vitale Brovarone et al., 2014b). These suites are exposed within a rather continuous metamorphic gradient from ~ 300 °C and $P < 1$ GPa to ~ 480 °C and 1.8 GPa (Agard et al., 2009; Gabalda et al., 2009; Schwartz et al., 2013; Vitale Brovarone et al., 2014b) (Fig. 1b).

In the investigated blueschist-facies units, whole rock carbon budgets in metasedimentary rocks unaffected by substantial fluid percolation show a general preservation of the initial marine carbonate and organic C concentrations and C stable isotope signature, pointing to little carbon mobilization during prograde metamorphism (Cartwright and Buick, 2000; Cook-Kollars et al., 2014). In this study we focus on channelized fluid pathways localized along the contacts separating mafic/ultramafic blocks and slices from the enclosing metasedimentary rocks. Previous work has documented the presence of fluid-mediated metasomatic halos along these contacts in the blueschist-facies units of Alpine Corsica. In particular, it has been shown that the metasedimentary rocks in contact with mafic/ultramafic rocks are characterized by the precipitation of metasomatic lawsonite (Vitale Brovarone et al., 2014a; Vitale Brovarone and Beyssac, 2014).

Equivalent processes are described in this work for in the equivalent blueschist-facies units of the W. Alps (Fig. 1b). In Alpine Corsica, this phenomenon was observed from minimum T conditions of about 370 °C and corresponding P of ~ 1-1.3 GPa up to the boundary with the underlying eclogite-facies unit at ~ 480 °C and 1.8 GPa (Fig. 1). No evidence for fluid-rock interactions and metasomatism was found within the same lithological suite at lower T in Alpine Corsica, and the T of ~ 370 °C was proposed as a regional-scale isograd for this process (Vitale Brovarone et al., 2014a). In the blueschist units of the Western Alps, evidence for this process was found from slightly lower T conditions of ~ 340 °C (Fig. 1). Owing to the more intense retrograde overprint and lawsonite breakdown in the Western Alps units compared to Alpine Corsica, only overprinted lawsonite metasomatic aureoles were identified at T > 400 °C (Fig. 1).

3. Methods

3.1. Sample collection and preparation

Rock samples were collected in the areas shown in Figure 1, which also presents the distribution of more than 230 outcrops identified in the two belts: > 200 outcrops in Alpine Corsica, part of which was already presented in Vitale Brovarone et al., 2014a, and 32 in the Western Alps (stars refer to main localities). About 80 samples from the two belts were selected for thin section preparation. Fourteen samples were collected from one selected reaction zone in Alpine Corsica (location in Fig. 1a) for detailed geochemical and Raman spectroscopy study. The samples were then cut to remove surface weathering. One chip of approximately 4x4x4 cm was isolated for each sample and cut into two parts for thin section preparation and bulk rock analysis, respectively. For bulk rock analysis, the samples were crushed and then pulverized with an agate mortar.

3.2. Bulk-rock C and trace element concentrations

Whole-rock analyses were performed at the Service d'Analyse des Roches et Minéraux (SARM, Centre de Recherches Pétrographiques et Géochimiques, Nancy, France). Total CO₂ concentration was analyzed using a LECO SC 144DRPC analyzer (LECO France, Garges les Gonesse, France) through calcination at 1400 °C. The uncertainty on the total CO₂ content is <10% for contents between 0.5 and 1%, <20% for contents between 0.5% and 0.1%, and >20% for contents <0.1% (detection limit 0.01%). Total organic C was analyzed following the same protocol after removal of all carbonates. The uncertainty on the total organic C (Corg) content is <15% for contents between 0.5 and 0.1% and >15% for contents <0.1% (detection limit 0.01%). The bulk inorganic C (carbonate minerals) content in the samples was calculated by subtracting the organic C from the total C. The results are presented in Table 1. The major and trace element analyses were done by alkali fusion of rock samples (LiBO₂), followed by concentration measurements using an ICP-OES Icap 6500 (ThermoScientific) for major elements, and an ICP-MS X7 (ThermoScientific) for trace elements (protocol by Carignan et al., 2001). The uncertainty on the elements used for mass balance calculations (see Section 5.2) are Hf: <10%, Th: <10%, and Zr: >5%.

3.3. Microscopic observations and Raman spectroscopy

Microstructural and petrographic characterizations were carried out on petrographic thin sections with an optical microscope first, and then by scanning electron microscopy (SEM). Petrographic thin sections were carbon coated for SEM work. Observations were performed at a working distance of 7.5 mm using a Zeiss Ultra 55 field emission gun SEM operated at 15 kV with a 120 µm aperture. Backscattered electron (BSE) mode was used to investigate chemical heterogeneities using an Angle Selective Backscattered Detector (AsB) or an Energy Selective Backscattered Detector (EsB).

Raman spectra were obtained using a Renishaw InVIA Reflex microspectrometer (IMPMC Paris). We used a 514 nm MODULASER argon laser in circular polarization. The laser was focused on the sample by a DMLM Leica microscope with a 100x objective (NA = 0.85), and the laser power at the sample surface was set around 1 mW. The Rayleigh diffusion was eliminated by edge filters, and to achieve a nearly confocal configuration, the entrance slit was closed down to 15 µm. The signal was finally dispersed using a 1,800 gr/mm grating and analyzed by a Peltier cooled RENCAM CCD detector. Before each session, the spectrometer was calibrated with a silicon standard. Because Raman spectroscopy of CM can be affected by several analytical mismatches, we followed closely the analytical and fitting procedures described by Beyssac et al. (Beyssac et al., 2002; 2003a). Measurements were taken on polished thin sections cut perpendicularly to the main fabrics, and CM was systematically

analyzed below a transparent adjacent/including mineral. The spectra were recorded in the extended scanning mode (700–2,000 cm^{-1}) with acquisition times from 30 to 60 s. The number of spectra for each sample is reported in Figure 3. Spectra were then processed using the software Peakfit using a linear baseline correction and simultaneous peak fitting with a Voigt function (Beyssac et al., 2002). The Raman results, expressed as R2 values (see Section 4.2 for details), are presented in Table 2.

3.4. Thermodynamic modeling

Thermodynamic modeling was used to estimate the solubility of CM at the considered metamorphic conditions and to assess the amount of aqueous fluid required to mobilize CM in the selected samples (Section 5.4). Molar fractions of H_2O , CO_2 and CH_4 in equilibrium with two types of CM for which thermodynamic data are available at the considered metamorphic conditions (Tumiati et al., 2020): an X-ray amorphous, glass-like C (Alpha Aesar, type I; hereafter glass-like C), and crystalline graphite. Based on the thermodynamic data of Tumiati et al. (2020), glass-like C has higher Gibbs free energy compared to graphite at P below around 3 GPa (T playing a minor effect), and consequently higher solubility. For this reason, these two types of CM were considered as reference for higher (glass-like C) and lower (graphite) CM solubility in aqueous fluids at the considered conditions. P–T conditions of 1.0 GPa–300°C, 1.3 GPa–370°C and 1.7 GPa–425°C — consistent with the regional, W-E metamorphic gradient in the considered terranes (Fig. 1) — were considered. The composition of fluids in equilibrium with glass-like C and graphite at the considered conditions have been retrieved using the routine "fluids" of the Perple_X package (Connolly, 1995) and the COH fluid EoS by Connolly and Cesare (1993). The CM in the model was considered to be chemically pure, with no heteroatoms such as N, S, and H. For each calculation, the $f\text{O}_2$ was buffered at conditions corresponding to the maximum activity of water (H_2O -maximum hereafter). The calculations were done at C saturation conditions owing to the presence of at least some CM throughout the reaction zones (Section 4.1). A rock density of 2.7 g/cm^3 was considered for the modeled metapelite. The augmented Gibbs free energy of formation of glass-like C has been modeled by setting the activity of C [$a(\text{C})$] in the calculations to values > 1 (Connolly, 1995). The moles of C dissolved in COH fluids, in equilibrium either with graphite or glass-like C, have then been compared with the moles of C leached out from the rocks (averaged to 67.5 mol/m^3 rock, corresponding to 0.03 wt.% graphite, see Section 4.1), yielding the amount of fluid (m^3) required to complete the dissolution process. The calculated fluid compositions are presented in Table 4.

4. RESULTS

4.1. Field and sample description

All collected samples exhibit a marked schistosity parallel to the contact with the mafic/ultramafic blocks. Next to the contact zone, the rocks show a marked bleaching of the metasediments. The thickness of the bleached aureole ranges from a few tens of cm to several meters and systematically matches with the precipitation of lawsonite. As a general feature, the bigger the mafic/ultramafic block, the thicker the metasomatic halo (Vitale Brovarone et al., 2014a). Several examples of these metasomatic rinds can be observed along the road joining Bocca a Serna and Morosaglia in Alpine Corsica (bottom part of the map in Fig. 1a). In the area of Colle dell'Agnello, Western Alps (Fig. 1b), the intersection between metasomatic aureoles rimming large mafic bodies and the topography locally defines large surfaces (tens of m) exposing the lawsonite-bearing, bleached rocks studied here (Fig. 3).

The general appearance of the bleached rocks is remarkably similar in the two belts (Figs. 2-4). A characteristic feature of the studied rocks is the presence of dark, CM-rich lawsonite crystals dispersed in a light-colored matrix mainly consisting of lawsonite + quartz + mica \pm chlorite (Fig. 4). Rocks showing these features were found only in the proximity of the above-mentioned lithological boundary, or, to a lesser extent, along thin (3-5 cm thick), foliation-parallel veins within the regional metapelitic schists (Fig. 2d-f).

In thin section, samples affected by partial bleaching clearly show the preservation of preexisting CM inside the newly formed lawsonite blasts (Fig. 4). For example, Figures 4a and 4e show the preservation of continuous of CM-rich layers of the metapelite inside the lawsonite blasts, and the partial to total bleaching of the same layers outside the blasts. More complex growth microstructures, such as hour-glass zoning highlighted by CM inclusions in the lawsonite blasts (Fig. 4c), are also observed in samples ranging from incipient to enhanced bleaching.

For detailed investigations, a ~ 2.5 m thick metasomatic aureole formed in metapelites in contact with a ~ 1 km long block of metagabbro was selected in Alpine Corsica (Fig. 5; see Figure 1a for location and Fig. S1 for complementary geological map). This aureole was selected owing to the absence of carbonate layers throughout the reaction zone, the presence of which would have hampered assessing the C budget across the reaction zone. The peak metamorphic conditions for this part of the blueschist-facies unit were estimated at ~ 420 - 430 °C and 1.6-1.8 GPa based on Raman Spectroscopy on Carbonaceous Material (RSCM) and thermodynamic modeling of CM-bearing metapelites unaffected by fluid-rock interaction (Vitale Brovarone et al., 2014b) (Fig. 1).

Across the interaction zone, the metapelite exhibits marked mineralogical variations and a decrease in CM content toward the adjacent metagabbro. Based on the microstructural and mineralogical features and CM content, five zones designed Z1 to Z5, are distinguished,

where the number in the designation indicates increasing intensity of metasomatism, i.e., proximity to the metagabbro. (Figs. 3-6). Zone Z1 (metapelite) mainly consists of white mica, quartz, chlorite, and titanite coexisting with CM, and does not show mineralogical/microstructural evidence for fluid-mediated transformations. The CM content (~0.14 wt.%, Fig. 5) fits the range of metapelitic schists in equivalent metasedimentary suites at comparable metamorphic conditions (Cook-Kollars et al., 2014). For these reasons, samples from Z1 are taken as the reference for characterizing the more intensely metasomatized zones.

Zones Z2 and Z3 both have a similar mineralogy compared to Z1, except for the fluid-mediated precipitation of large syn-to-post kinematic lawsonite blasts and for different modal proportions (Fig. 5). In Z2, a slight decrease of CM relative to Z1 is observed in the most internal sample, i.e. towards the metagabbro, even though heterogeneous, foliation-parallel bleaching was observed within single thin sections. Carbonaceous material is homogeneously distributed between the matrix and as inclusions in lawsonite and titanite. This feature demonstrates that the CM inclusions in lawsonite represent pre-existing CM rather than fluid-deposited CM. Zones Z2 and Z3 were distinguished because of a sharp decrease in the CM content from Z2 (~0.12 wt.%) to Z3 (~0.03 wt.%, Figs. 4, 5), and for slightly higher amounts of quartz in Z3. Zone Z3 titanite and lawsonite blasts are dark and contain abundant inclusions of CM, similar to those in Z2, but the surrounding matrix is lighter in color and contains less CM relative to Z1 and Z2. Moreover, lawsonite in Z3 commonly shows a CM-rich core and a CM-poor/free rim, suggesting that the CM removal happened during the lawsonite precipitation event at high-pressure conditions (Figs. 3, 7d).

Zone Z4 mainly consists of quartz and albite (late pseudomorphic product after blue amphibole), together with local mica-chlorite microlithons and corroded titanite and lawsonite. Lawsonite forms large (similar to Z2-Z3) crystals that appear extensively replaced by quartz (Fig. 7f). Nevertheless, a second generation of tiny, idioblastic lawsonite crystals is also observed (Fig. 7f). The CM content of Z4 is below detection limit for bulk measurements (<0.01 wt.%), and is mainly found as inclusions in lawsonite and titanite relicts. Matrix CM in Z4 is very rare and occurs as scattered individual grains.

Zone Z5 has a metagabbro-like mineral assemblage (see below for details regarding its metasedimentary origin) and mainly consists of blue amphibole, chlorite and titanite, the titanite being generally inclusion-poor and petrographically different from that in Z1-Z4. The blue amphibole is only partially retrogressed to albite. As in Z4, the CM content of Z5 is below detection limit (<0.01 wt.%).

Despite the mineralogical variations in Z4-Z5 compared to Z1-Z3, including the formation and transformation of blue amphibole and partial replacement of lawsonite testifying to a

complex metasomatic evolution, the sedimentary origin of the Z4-Z5 rocks is indicated by the rare earth element (REE) patterns. The REE patterns of these rocks are in fact consistent with all other altered and unaltered metapelite-derived zones (Z1-Z3), and clearly differ from the adjacent metagabbro (Fig. S2; Table S1). The metasedimentary origin of Z4-Z5 is also supported by the presence of CM inclusions in titanite (Z5 in Fig. 8). No carbonate was detected by optical and electron microscopy in the studied samples, including in the metagabbro. In one sample, however, the presence of tiny amounts of carbonate is inferred based on the presence of total CO₂ other than CM in the bulk rock analysis (Fig. 5). In the metagabbro, no CM was detected by optical microscopy and the bulk rock CM content is at detection limit (0.01 wt.%) or lower (Table 1). A slight increase of bulk total CO₂ is observed in the metagabbro close to the metasediment, but the bulk concentration remains very low (\leq 0.09 wt.%) (Table 1).

4.2. Raman spectroscopy of CM across the reaction zone

In order to investigate the patterns and mechanisms of CM removal in the studied samples, a Raman spectroscopy study was carried out to characterize the nature of CM across the reaction zone. The degree of graphitization of CM can be quantified by the relative area of the G, D1, and D2 band of CM in Raman spectra (Fig. 7a-c) (e.g., Beyssac et al., 2002). This is expressed by the D1/(G + D1 + D2) peak area ratio, hereafter referred to as the R2 ratio (Beyssac et al., 2003b); the lower the R2, the more graphitic the CM, with perfectly ordered CM having a R2 value equal to 0 (no defect band) (Fig. 7a-c). For reference, CM heated under regional metamorphic conditions shows the following T-R2 correspondences: 350 °C \simeq 0.7; 450 °C \simeq 0.4; 550 °C \simeq 0.2; 650 °C and above \simeq 0 (Beyssac et al., 2002).

The results of the Raman analysis are presented in Figure 8 and Table 2 as a function of the measured R2 values across the reaction zone. The Raman characterization of CM in this study is aimed at assessing the mode of fluid-CM interaction and removal of bulk CM rather than constraining metamorphic T conditions by RSCM thermometry, which is published elsewhere (Vitale Brovarone et al., 2014b). Nevertheless, for reference, the R2 value of CM in the regional metapelite unaffected by fluid infiltration next to the studied metasomatic aureole typically 0.4-0.6 (Z1 Fig. 8), and corresponds to about 400-450 °C (Fig. 1a).

Both CM included in HP minerals such as lawsonite and titanite (CM_{Inc}) and matrix CM (CM_M) were analyzed throughout the reaction zone (Fig. 7d-f, 8). CM_{Inc} in titanite (Z1) and lawsonite (Z2 to Z4) yield rather constant R2 values ranging from 0.4-0.6 (100% of the analyzed CM_{Inc} in Z1; 86% in Z2; 92% in Z3; 100% in Z4). These R2 values match the degree of graphitization of metamorphosed CM observed in non-metasomatized metapelites from the same metamorphic unit. In Z2 and Z3, minor clusters, each < 10% of the analyzed

CM_{Inc}, are also present for R2 < 0.2, 0.3-0.4, and ~ 0.6-0.7 (Fig. 8). Conversely, CM_{Inc} in titanite from Z5 yields a much lower R2 cluster < 0.2 (80%) and two subordinate clusters at 0.2-0.3 (5%) and 0.3-0.4 (15%). Compared to CM_{Inc}, CM_M shows a progressive decrease from Z1 to Z4. In Z1, CM_M yields values that are reasonably consistent with those for CM_{Inc}, with ~ 88% of the analyses clustering at the regional R2 range of 0.4-0.6; in addition, ~ 10% of the spot analyses cluster at 0.3-0.4 and ~ 2% at > 0.2. In Z2, the regional R2 cluster (0.4-0.6) in CM_M decreases to ~ 68% of the spot analyses, while the 0.3-0.4 cluster increases to ~ 30%. A small cluster > 0.2 (~ 2%) is also present. In Z3, the regional R2 cluster (0.4-0.6) in CM_M further decreases to ~ 58%. The 0.3-0.4 cluster decreases to ~ 22%, and both the > 0.2 cluster and a new cluster at 0.2-0.3 increase to ~ 9% each. In Z4, the regional R2 cluster (0.4-0.6) in CM_M drops to ~ 4% of the spot analyses, the 0.3-0.4 cluster further decreases to ~ 9%, whereas the > 0.2 cluster dominates at ~ 87%. No CM_M was found in Z5.

4.3. Geochemical variations across the reaction zone

Figure 9 shows a concentration ratio diagram where the composition of samples from Z2 to Z5 (metasomatized rocks) is normalized to the average composition of samples from Z1 (protolith rock). Samples of metagabbros close to the contact are normalized to a least altered sample of metagabbro collected at 5.40 m from the contact (sample 29). Across the metapelite-metagabbro contact, K, B, Cs and Rb exhibit a marked depletion in the altered samples relative to the least altered precursor rocks. Lead shows depletion in the metagabbro and an irregular pattern in the metapelite, plausibly representing heterogeneity in bulk sulfide content. Calcium and Sr have similar, yet complex patterns. The metagabbro shows a general depletion in Ca and Sr, except for the most altered sample next to the contact zone. In the metapelite, Ca and Sr initially increase in Z2-Z3 and then decrease in Z4-Z5, but still remaining enriched relative to Z1. In Z5, a decoupling between Ca and Sr is observed, with a slight increase in Ca and a decrease in Sr relative to Z4. Sodium has a different behavior compared to the other considered elements. The altered metagabbro samples show a progressive depletion in Na towards the contact, whereas the opposite trend is observed in the metapelite.

5. DISCUSSION

5.1. Timing and mechanism of fluid-mediated CM dissolution

The systematic decrease bleaching of metasedimentary rocks along lithological boundaries, as well as the detailed microstructural features across the selected metasomatic halo indicate that the observed decrease in CM across the investigated lithological boundary is the result of a

fluid-mediated process that happened at HP conditions in the subduction zone. The studied lithological juxtaposition have been interpreted as inherited, oceanic tectonic or sedimentary structures only slightly reworked by the Alpine tectonics (Lagabrielle et al., 2015; Vitale Brovarone et al., 2014b). This indicates that the observed metasomatic features along lithological boundaries formed in response to fluid-mediated processes rather than contact metamorphic (e.g., magmatic injection) processes. Primary variations in the bulk CM content inherited from the protolith rocks may also be present locally but cannot explain the systematic patterns documented along several tens of lithological boundaries of various nature (Figs. 1-5). The detailed characterization of one reaction zone presented in Figures 5-8 clearly indicates that CM was initially present throughout the reaction zone and progressively removed towards the contact with the adjacent metagabbro (see Section 4.1). The preservation of characteristic microstructures of the protolith CM-bearing pelitic schist within the fluid-deposited lawsonite blasts (Fig. 4) also indicates that the CM inclusions in lawsonite represent relicts of the CM initially present in the rock. The Raman analysis additionally confirms that the relict CM preserved as inclusion in lawsonite/titanite across the reaction zone is analogous to the CM of the starting metapelitic rock (Fig. 8). This feature rules out the possibility that the CM inclusions precipitated from the fluid together with the host lawsonite. The observed microstructural patterns of CM depletion in Z3, e.g. CM-rich lawsonite cores and CM-free lawsonite rims, also suggest that the CM leaching happened during the same metasomatic event responsible for the precipitation of lawsonite. This event has been constrained to HP/LT conditions on the basis of distribution along a regional-scale metamorphic isograd (Vitale Brovarone et al., 2014b; 2014a). The initial precipitation of lawsonite in the reaction zone (preserved in Z2-Z4) and associated H₂O increase (Vitale Brovarone and Beyssac, 2014) indicate that the fluid responsible for the removal of CM was dominantly aqueous.

The geochemical patterns across the reaction zone provide insights into the driving mechanism for CM leaching. Two alternative hypotheses are discussed: a redox gradient between the two adjacent lithologies in a static fluid, or the infiltration of an external fluid. In the first case, the dominant mechanism of mass transport is diffusion, and a chemical gradient between the metagabbro and the metapelite is expected. Conversely, a more complex pattern potentially including selective mass loss/gain in both lithologies may result from fluid-rock interaction mediated by advection of an external fluid. In the selected metasomatic halo (Fig. 5), a chemical gradient controlled by diffusion in a “closed” metasediment-metagabbro system would require some kind of C reprecipitation at the contact between the two lithologies or in the metagabbro, which is not observed (Fig. 6). The general behavior of fluid-mobile elements such as K, Rb, Ba and Cs across the reaction zone is characterized by a marked mass loss on both sides of the contact. Na may suggest a diffusive exchange between

the metagabbro and the metapelite (Fig. 9). Nevertheless, the behavior of Na, as well as Ca and Sr, may reflect different fluid-rock equilibration between the fluid and either the metapelite or the metagabbro, perhaps involving some component of mechanical dispersion. Moreover, coupling the Ca and Sr profiles with the observed mineralogical evolution across the contact suggests a protracted fluid-rock reequilibration with initial precipitation (preserved in Z2-Z3) and successive destabilization (Z4-Z5) of lawsonite (see Section 4.1 for details). As a whole, the above evidence suggests a dominantly advective mechanism of mass transport from an external fluid source.

The field data also suggest that the externally-derived fluid was primarily channelized parallel to the regional schistosity. Individual samples at the transition from Z2 to Z3 show discrete, foliation-parallel zones of bleaching. Moreover, the individual CM-leached, lawsonite-bearing veins identified within the metasedimentary pile are also parallel to the regional schistosity (Fig. 2c). This feature is in agreement with several previous studies indicating that fluid flow is greatest parallel to lithological boundaries or foliations (Ague, 2014 and references therein).

During progressive loss of CM from the rock, the fluid must have been at least transiently enriched in C. Increases in fluid C concentration may have affected the stability of mineral assemblages within the reaction zone. For example, increasing C content in the fluid may favor the breakdown of lawsonite (Nitsch, 1972), which occurred at least transiently in Z4 (Section 4.1). The formation of CO₂ may also lower the solubility of SiO₂ in metamorphic fluids (Newton and Manning, 2009), which could explain the increase of quartz modal amount in Z4. Nevertheless, recent experimental studies suggest that CO₂ in graphite-saturated COH systems may strongly increase in the presence of aqueous SiO₂ and the formation of organic complexes (Tiraboschi, 2018; Tumiati et al., 2017). Following these results, the extensive quartz precipitation in Z4 may be ascribed to a process of C dilution in the fluid by either infiltration of aqueous fluids, or the in-situ breakdown of metasomatic lawsonite.

5.2. Selective dissolution of subducted disordered CM

Our data indicate that the more disordered CM component of the studied samples was more affected by the fluid infiltration than the crystalline CM. This phenomenon requires consideration of the origin of the two CM types and the related implications for bulk CM dissolution. Based on observations from both present-day sedimentary basins and metamorphic complexes, the CM present in metasedimentary rocks may have three different origins. The first and most common type is the metamorphosed biomass of the protolith sedimentary rock. The second type is the so-called detrital CM, which derives from the

erosion of exposed CM-bearing rocks, burned organic material, or any other source of CM-bearing materials. Studies conducted in active sedimentary environments indicate that detrital CM preserved in sediments is typically rather crystalline (low R_2 values) (Bouchez et al., 2010; Galy et al., 2008). The third type is graphitic C deposited by C-saturated fluid (Cesare, 1995; Galvez et al., 2013).

The Raman analysis across the selected reaction zone indicates the presence of two CM populations being characterized by either disordered CM (high R_2) and nearly crystalline graphite (low R_2) (Fig. 8). The presence of these two populations throughout the reaction zone, including in the metapelite unaffected by fluid-mediated transformations, indicates they were already present in the rock prior to the fluid infiltration. The disordered CM cluster is interpreted to represent metamorphosed biomass, whereas the more crystalline CM cluster most likely represents inherited detrital CM. Other interpretations, such as fluid-deposited graphite, would be incompatible with the observed microstructural, mineralogical, and Raman patterns.

Based on the above considerations, the observed patterns of fluid-mediated CM dissolution may be dependent on the initial concentrations of inherited crystalline CM in the rock relative to more disordered CM. Taking Z5 CM as a proxy for the bulk detrital CM content because this zone has no disordered CM left, the bulk concentration of detrital crystalline CM in the original metapelite was < 0.01 wt.% (below detection limit). Because Z4 samples, also containing CM > 0.01 wt.%, are much darker and CM-rich than Z5 (based on optical microscope comparison), it is plausible that the actual concentration of detrital crystalline CM is probably $\ll 0.01$ wt.%.

Following the method of Ague (1994) and by considering Zr as the least mobile element in this system (Ague, 2017; Zhang et al., 2018), the fractional CM loss across the reaction zone was estimated for each reaction zone relative to Z1 (Table 3). An assumption was made that the initial CM content was similar throughout the reaction zone, as suggested by the comparable microstructural distribution of CM inclusions in lawsonite and titanite from Z2 to Z5.

In the most CM-depleted zones the CM concentration is below detection limits, and the mass balance calculations require some assumptions. In these samples, the initial concentration of disordered CM was estimated by considering the proportion of more disordered CM ($R_2 > 0.2$) relative to more crystalline CM ($R_2 < 0.2$) in the studied samples as deduced by Raman spectroscopy (Fig. 6) with respect to the detection limit (0.01 wt.%). The calculation yielded CM loss of 18% (± 38) in Z2, 84% (± 8) in Z3, $> 86\%$ (± 2) in Z4, and $> 90\%$ in Z5 (all relative to Z1). The resulting CM mass loss for 100 g of rock relative to Z1 is 0.03 g (± 0.05) in Z2, 0.12 g (± 0.01) in Z3, and > 0.12 g and > 0.13 g in Z4 and Z5, respectively (CM content

in Z4–Z5 is below detection limits). The higher uncertainty in the weakly altered Z2 is most probably explained by primary heterogeneities larger than the mass change, and/or the amount of mass change was heterogeneously distributed within Z2. At least the latter hypothesis was observed within a single thin section of Z2, with CM leaching being more pronounced along discrete foliation-parallel layers (Fig. 5). For comparison, fractional CM loss across the reaction zone was also calculated considering Hf and Th as the least-mobile elements and yielded very similar results to Zr (Table 3). The calculations are actually fairly insensitive to the reference element chosen for Z3–Z5 because the percentages losses of CM are so large.

5.3. Fluid-rock regime of CM dissolution

As previously observed in sedimentary environments (Bouchez et al., 2010; Galy et al., 2008) and predicted for metamorphism (Connolly, 1995; Ziegenbein and Johannes, 1980), the response of CM to fluid-rock interactions may be different depending upon its degree of graphitization (Souche et al., 2012). From a thermodynamic point of view, disordered CM is a metastable phase during metamorphism, and a fluid in metastable equilibrium with such material is theoretically enriched in C compared to pure/crystalline graphite (Ziegenbein and Johannes, 1980) (Tumiati et al., 2020). Flushing of this material by aqueous fluids and protracted fluid-rock equilibration is therefore expected to selectively remove disordered CM from the rock with respect to a more crystalline CM, and our Raman spectroscopy dataset confirms this theoretical assumption. Nevertheless, the widespread preservation of disordered CM in the regional metapelitic rocks unaffected by strong fluid-rock interaction indicates that this expectation becomes relevant only in the case of major fluid infiltration; the approximation of CM to pure graphite for thermodynamic calculations appears to be reasonable in closed systems.

Equilibria between fluids and CM have been classically described in the COH system (Connolly, 1995; Holloway, 1984). In this system, any fluid in equilibrium with CM is expected to lie on a metastable CM-saturation curve. The position of the curve is dependent on the P and T conditions, and on the crystallinity of the CM (Ziegenbein and Johannes, 1980). The concentration of C in a graphite-saturated COH fluid in equilibrium with CM increases with increasing T, with decreasing P, and/or with decreasing crystallinity of the CM. An increase in CM crystallinity, in the case of subduction metamorphism, would also require an increase in T.

Therefore, the observed CM leaching could be explained by an infiltrating fluid migrating along either an up-T or a down-P gradient. Up-T fluid circulation has been proposed in the metamorphic units of Alpine Corsica, but within inherited fractures unrelated to the regional

foliation (Vitale Brovarone et al., 2018b). In the present case, field relationships suggest that the fluid flow was dominantly foliation-parallel, which in a simple slab thermomechanical configuration would correspond to a slab-parallel, down-T flow. However, because a down-T, down-P flow would lead to C precipitation rather than leaching (Cesare, 1995), an up-dip fluid flux along a rather constant T (i.e., along a slab parallel geotherm) is the most likely condition to dissolve C at the considered conditions.

Alternatively, or complementary to an isothermal up-dipgradient, another mechanism can be proposed based on the recent experimental and thermodynamic results by Tumiatì et al. (2017). The authors showed that the C concentration in a graphite or, more generally, CM-bearing system can vary by 30% in the presence of dissolved SiO₂ relative to a pure COH system, and without significant variations in fO_2 . This was explained by the formation of organosilicon complexes in the fluid (Tumiatì et al., 2017). The complex evolution of the studied metasomatic aureole preserved from Z2 to Z5 clearly documents fluid-rock variations involving initial lawsonite precipitation (preserved in Z2) and successive consumption (Z3-Z5). The precipitation of abundant quartz in Z3-Z5 demonstrates aqueous SiO₂ oversaturated conditions that could have favored the extreme CM depletion in the same zones. We therefore propose that the mechanism of fluid-mediated CM removal was driven by either a down-P gradient, or by modifications of the dissolved SiO₂ in the fluid-rock system, or a combination of them.

5.4. Fluid fluxes responsible for selective CM dissolution

The removal of disordered CM relative to the more crystalline CM allows assessment of the aqueous fluid fluxes required to achieve the observed CM removal in the field area. Flux estimates were calculated based on the predicted C solubility in fluids in equilibrium with either crystalline graphite (lower solubility) and glass-like C (higher solubility) (Tumiatì et al., 2020; see section 3.4 for details). Glass-like C is not expected to be present in natural samples of metamorphic rocks but is considered here as a low solubility reference compared to graphite based on the available thermodynamic data at the considered P-T conditions (Tumiatì et al. 2020). Under the assumption that the studied CM was chemically pure (see Section 3.4), the observed selective removal of disordered CM indicates that this phase was metastable relative graphite. This would imply that the disordered CM was more soluble than graphite. However, because thermodynamic data for the disordered CM present in the natural samples are not available, the higher or lower solubility of this material relative to the glass-like C used by Tumiatì et al. (2020) cannot be assessed. The range of CM solubility considered in this study therefore provides a qualitative constrain on the magnitude of

aqueous fluid infiltration responsible for the selective removal of disordered CM relative to more crystalline CM.

Calculations at H₂O-maximum conditions were done at three different sets of P and T conditions: 300 °C and 1 GPa, 370 °C and 1.3 GPa, and 425 °C and 1.7 GPa. These correspond to low-T prograde conditions, the regional isograd of lawsonite metasomatism and associated CM leaching, and the peak metamorphic conditions of the selected samples, respectively (Section 3.4). Based on the thermodynamic model of Tumiati et al. (2020), the solubility of glass-like C is 23% higher than graphite at 300 °C/1 GPa, 21% higher at 370 °C/1.3 GPa, and 18% higher at 425 °C and 1.7 GPa.

As introduced above, the disordered CM component present in the studied rocks is expected to be less soluble than glass-like C, and more soluble than graphite. The following discussion is therefore not intended to be quantitative on the amount of fluid flux, but rather to assess the patterns of selective leaching of disordered CM (this section) and the magnitude of fluid flux (Section 5.5).

Table 4 shows the calculated cumulative volumes of H₂O required to mobilize either graphite or glass-like C according to the calculated fractional mass losses per m³ of rock (Section 5.2). The resulting water:rock ratio area also shown (Table 4). For a given *f*O₂ buffer such as the H₂O-maximum, these ratios are conservative as only the fraction of fluid required to mobilize the CM was considered. As water:rock ratios provide only partial information on the mechanisms of fluid/rock interaction, the time-integrated fluid fluxes (Ague, 2014; Baumgartner and Ferry, 1991) required to achieve the observed CM losses were estimated across the reaction zone as discussed in Section 3.3.

Time-integrated fluid fluxes (q_{TI}) are calculated with equation 21 in Ague (1998) that is valid for advection dominated systems with small porosity ($\phi < 0.01$):

$$q_{TI} = L_{GF} \frac{m_i}{(C_i^{eq} - C_{i,x=0}^{input})}$$

Where L_{GF} is the distance of the geochemical front propagation, m_i is the number of moles of carbon consumed per unit volume (mol m⁻³) estimated from mass balance analysis, C_i^{eq} is the fluid composition that would be in equilibrium with the mineral assemblage, and $C_{i,x=0}^{input}$ is the initial fluid composition. C_i^{eq} corresponds to the experimentally determined solubility of either glass-like C or graphite (Tumiati et al, 2020), whereas $C_{i,x=0}^{input}$ is set to zero in order to have the most conservative results. Results are presented in Table 5.

The results, shown in Figure 10, are dependent on the distance of reaction front propagation (L), which corresponds to the distance of fluid percolation parallel to the lithological boundary. The parameter n on the vertical axis is the log₁₀ of L expressed in meters. For example, for L = 10 m, n = 1.

Three general patterns are observed: (i) the time-integrated fluid fluxes (q_{TI}) required to achieve the observed CM losses decrease with increasing T and P, in agreement with the general behavior of the COH system at C-saturated conditions (Connolly, 1995; Holloway, 1984); (ii) at a given P-T condition, the flux is higher for graphite relative to glass-like C, in agreement with earlier studies (Ziegenbein and Johannes, 1980); and (iii) the Δq_{TI} between graphite and glass-like C ($\Delta q_{TI_{\text{graphite-glass-like C}}}$) decreases with increasing P (and T to a lesser degree, Tumati et al., 2020). More specifically, the $\Delta q_{TI_{\text{graphite-glass-like C}}}$ is of the order of $1.8 \cdot 10^n \text{ m}^3/\text{m}^2$ at 300 °C and 1 GPa, $0.8 \cdot 10^n \text{ m}^3/\text{m}^2$ at 370 °C and 1.3 GPa, and $0.5 \cdot 10^n \text{ m}^3/\text{m}^2$ at 425 °C and 1.7 GPa.

The profiles in Figure 10 also indicate that the fluid flux was higher close to the lithological boundary and progressively decreased towards the metasedimentary rocks in a way consistent with the numerical simulations of Ague (2007) for fluid flow in mélange systems. Variations in the size and geometry of the reaction zone and magnitude of fluid flux are expected depending on the size and shape of the blocks (Ague, 2007).

The above calculations show that degree of CM crystallinity has a lower effect on the selective dissolution of disordered CM at P-T conditions of 1.7 GPa and 425°C (peak conditions for the selected aureole) relative to lower-grade conditions (Fig. 10). The field isograd for the companion lawsonite metasomatism and CM leaching suggests that this fluid-mediated process took place at conditions of ~ 370 °C and ~ 1.3 GPa in Alpine Corsica. At these conditions, the $\Delta q_{TI_{\text{graphite-glass-like C}}}$ is slightly higher compared to peak conditions (Fig. 10). We therefore suggest that the selective leaching was achieved during the prograde path of the selected rocks where the difference in solubility between disordered CM and graphite was higher. In the Western Alps, evidence for CM leaching in equivalent lithological contexts was observed at lower T in the range of 340 °C (Fig. 1), suggesting slightly different regional fluid flow patterns, but likely similar orders of magnitude compared to Corsica, as discussed in the next section.

5.5. Insights on the magnitude of intra-slab fluid flow along lithological boundaries

The above mass balances provide information on the magnitude of fluid flux channelized along lithological boundaries under blueschist-facies conditions in subduction zones. Although the flux estimates presented in the previous section refer to the CM loss measured in one metamorphic alteration profile, the general patterns of CM leaching observed at the regional scale in Alpine Corsica and Western Alps equivalents plausibly suggest comparable orders of magnitude. Considering the exposed length of the metasediment-metagabbro contact (~ 1 km) as a value for L, the time-integrated fluid fluxes would increase by three orders of magnitude compared to the values reported in Figure 9 (i.e., $n = 3$) and reach values as high as

10⁶ m³/m² in Z5 (~0.8 m in thickness). This clearly indicates conditions of channelized fluid flow along conduits (see Ague, 2014 for comparison with flux estimates in various crustal settings). The dependency of the time-integrated fluid flux on the length of the reaction front is also consistent with the observation that the thickness of the reaction zone is qualitatively correlated with the size of the mafic/ultramafic block (Vitale Brovarone et al., 2014a). Moreover, because of permeability contrast, the largest fluxes will be concentrated around the margins of the largest blocks (Ague, 2007).

Figure 11 qualitatively describes the fluid flux distribution in the investigated block-in matrix lithological suite, at different depths. The same concept can apply to tectonic mélange complexes (Ague, 2007). For example, evidence for CM leaching in metasedimentary rocks is reported in an ultramafic mélange in Japan (Mori et al., 2014). Even though the order of magnitude of the time-integrated fluid fluxes is similar at the three chosen P-T conditions, according to Figure 10, it is expected that the fluid fluxes along lithological boundaries progressively decrease with depth.

The distribution of the observed fluid-mediated processes along lithological boundaries or as individual channels (both parallel to the regional foliation) suggests that potentially large amounts of subduction zone fluids can migrate up-slab, thus limiting the amount of fluid transferred to the mantle wedge (Angiboust et al., 2014; Piccoli et al., 2016; Wilson et al., 2014).

5.6. Role of fluid-mediated dissolution of graphitic C to subduction C fluxes

Subducted CM is generally considered to be largely retained in the rock during prograde metamorphism, as indicated by regional-scale analysis of metamorphosed oceanic sediments in orogenic belts (Cook-Kollars et al., 2014). However, experimental results indicate that CM, including crystalline graphite, is indeed soluble in aqueous fluids at metamorphic conditions (Tumiati et al., 2017; 2020), making it susceptible to fluid-mediated mobilization along permeability channels. Our study confirms that subducted CM can be mobilized along channelized fluid pathways at forearc conditions. Although our results support a general preservation of highly crystalline CM at P and T conditions not exceeding 1.7 GPa and 425°C, only slight variations relative to the estimated fluxes would result in removal of crystalline graphite. It is not excluded, at least in Z5 of the studied natural profile, that some of the more graphitic CM was actually removed from the rock. In any case, the fluid-mediated dissolution of CM documented in this study, as well as the experimental data by Tumiati et al. (2020), suggests that a region of potential release of significant amounts of C through fluid-mediated mobilization of disordered CM may exist in subduction zones. Mass balance

analysis shows that nearly complete removal of CM can happen in metapelitic rocks adjacent to lithological boundaries channelizing aqueous fluids (Table 3). Field relationships and numerical models indicate that the thickness of bleached zones is function of the length of the lithological boundary, or, in other words, the length of the fluid channel (Ague, 2007). In the present case studies. Prograde infiltration of aqueous fluids through rocks containing disordered CM may therefore exert a negative feedback on the sink of refractory C-bearing phases into the mantle by subtracting a fraction of the subducted organic C from the rock prior to full graphitization.

The significance of this process on global carbon fluxes would depend on the extent and distribution of metasediment-hosted fluid channels. The studied field areas suggest that these channels can be very common within lithologically heterogeneous metamorphic units (Fig. 1), such as subducted sedimentary mélanges or plate-interface tectonic mixings. Similarly, fluid channelized along the top of the subducting slab, or along the base of the slab sedimentary rocks, has potential to mobilize significant amounts of reduced C. Flushing of metapelitic rocks by graphite-undersaturated reduced aqueous fluids, for example generated by hydration (Vitale Brovarone et al., 2017) or dehydration (Piccoli et al., 2019) of ultramafic rocks in the subduction zone, may enhance the dissolution of CM relative to more oxidized fluids (Connolly, 1995). In the absence of significant carbonate minerals, dissolution of CM may impart a light $\delta^{13}\text{C}$ signature to the slab-derived fluids transferred to shallower reservoirs. Considering the $\delta^{13}\text{C}$ signature of CM at the relevant metamorphic conditions in carbonate free metasediments of $\sim -25\text{‰}$ (Cook-Kollars et al., 2014), and the fluid speciation of graphite-saturated systems at the H_2O -maximum, the fluid generated by the CM dissolution would have $\delta^{13}\text{C}$ of $\sim -25\text{‰}$ and -23‰ at 300 °C and 425 °C , respectively (graphite- CO_2 and graphite- CH_4 fractionation factors from Bottinga et al 1969). If the process of CM dissolution happens through infiltration of graphite-undersaturated reduced fluids, the resulting fluids would be even lighter. A possible natural example of generation and circulation of such fluids are documented by Spandler et al. (2008), who reported isotopically light, fluid-deposited carbonate (as low as -12‰) in metasomatized sequences from the metamorphic belt of New Caledonia. In the same terrane, metasedimentary rocks are CM-depleted compared to equivalent sequences unaffected by intense fluid circulation (Vitale Brovarone et al., 2018a).

6. CONCLUSIONS

We collected field, microstructural, geochemical, and thermodynamic data showing that channelized, fluid-mediated dissolution of CM can be an efficient process at forearc depth in subducting slabs. Our study shows that, within individual samples, the removal of CM was more efficient for disordered CM relative to crystalline CM, providing a means to constrain

the magnitude of fluid fluxes at different depths within the subducting slab. The data collected herein indicate that the order of magnitude of fluid fluxes along channelized pathways at blueschist-to-eclogite-facies conditions is large enough to potentially remove the entire amount of organic C from a given volume of rock, but only in the presence of channelized fluid flow. The widespread distribution of fluid-mediated removal of CM along lithological boundaries in two investigated mountain belts indicates that the estimated magnitude of channelized fluid-fluxes can be common in the forearc regions of subduction zones where subducted CM is structurally disordered. This fluid-mediated process is expected to mobilize significant amounts of isotopically light, reduced C along the top of the slab or at the base of the subducted sedimentary crust.

Acknowledgements

We would like to thank Balz Kamber for editorial handling and two anonymous reviewers for their comments on our study. This work benefited from financial support by LabEx Matisse, ANR-T ERC, MIUR Levi Montalcini program, CNRS - INSU (Syster program), and Emergence de la ville de Paris program. Support by the Deep Carbon Observatory (DCO) is also acknowledged. Scanning Electron Microscope (SEM) facility of the Institut de Minéralogie, de Physique des Matériaux et de Cosmochimie is supported by Région Ile de France grant SESAME 2006 N_ I-07-593/R, INSU-CNRS, INP-CNRS, University Pierre et Marie Curie – Paris 6, and by the French National Research Agency (ANR) grant no. ANR-07-BLAN-0124-01.

REFERENCES

- Agard, P., Jolivet, L., Goffé, B., 2001. Tectonometamorphic evolution of the Schistes Lustrés complex: implications for the exhumation of HP and UHP rocks in the Western Alps.
- Agard, P., Monié, P., Jolivet, L., Goffé, B., 2002. Exhumation of the Schistes Lustrés complex: in situ laser probe $^{40}\text{Ar}/^{39}\text{Ar}$ constraints and implications for the Western Alps. *Journal of metamorphic Geology* 20, 599–618. doi:10.1046/j.1525-1314.2002.00391.x
- Agard, P., Yamato, P., Jolivet, L., Burov, E., 2009. Exhumation of oceanic blueschists and eclogites in subduction zones: Timing and mechanisms. *Earth Science Reviews* 92, 53–79. doi:10.1016/j.earscirev.2008.11.002
- Ague, J.J., 2017. Element mobility during regional metamorphism in crustal and subduction zone environments with a focus on the rare earth elements (REE). *American Mineralogist* 102, 1796–1821. doi:10.2138/am-2017-6130
- Ague, J.J., 2014. Fluid Flow in the Deep Crust, in: *Treatise on Geochemistry*. Geological Society of America, pp. 203–247. doi:10.1016/B978-0-08-095975-7.00306-5
- Ague, J.J., 2007. Models of permeability contrasts in subduction zone mélange: Implications for gradients in fluid fluxes, Syros and Tinos Islands, Greece. *Chemical Geology* 239, 217–227. doi:10.1016/j.chemgeo.2006.08.012
- Ague, J.J., Nicolescu, S., 2014. Carbon dioxide released from subduction zones by fluid-mediated reactions. *Nature Geoscience* 7, 355–360. doi:10.1038/ngeo2143
- Angiboust, S., Agard, P., Jolivet, L., Beyssac, O., 2009. The Zermatt-Saas ophiolite: the largest (60-km wide) and deepest (c.70-80 km) continuous slice of oceanic lithosphere detached from a subduction zone? *Terra Nova* 21, 171–180. doi:10.1111/j.1365-3121.2009.00870.x

- Angiboust, S., Pettke, T., De Hoog, J.C.M., Caron, B., Oncken, O., 2014. Channelized Fluid Flow and Eclogite-facies Metasomatism along the Subduction Shear Zone. *Journal of Petrology* 55, 883–916. doi:10.1093/petrology/egu010
- Balestro, G., Festa, A., Tartarotti, P., 2015. Tectonic significance of different block-in-matrix structures in exhumed convergent plate margins: examples from oceanic and continental HP rocks in Inner Western Alps (northwest Italy). *International Geology Review* 57, 581–605. doi:10.1080/00206814.2014.943307
- Baumgartner, L.P., Ferry, J.M., 1991. A model for coupled fluid-flow and mixed-volatile mineral reactions with applications to regional metamorphism. *Contributions to Mineralogy and Petrology* 106, 270–285.
- Beltrando, M., Lister, G.S., Rosenbaum, G., Richards, S., Forster, M.A., 2010. Recognizing episodic lithospheric thinning along a convergent plate margin: The example of the Early Oligocene Alps. *Earth Science Reviews* 103, 81–98. doi:10.1016/j.earscirev.2010.09.001
- Beyssac, O., Goffé, B., Chopin, C., Rouzaud, J.-N., 2002. Raman spectra of carbonaceous material in metasediments: a new geothermometer, *Journal of Metamorphic Geology*.
- Beyssac, O., Goffé, B., Petitet, J.-P., Froigneux, E., Moreau, M., Rouzaud, J.-N., 2003a. On the characterization of disordered and heterogeneous carbonaceous materials by Raman spectroscopy. *Spectrochimica Acta Part A: Molecular and Biomolecular Spectroscopy* 59, 2267–2276. doi:10.1016/S1386-1425(03)00070-2
- Beyssac, O., Goffé, B., Petitet, J.-P., Froigneux, E., Moreau, M., Rouzaud, J.-N., 2003b. On the characterization of disordered and heterogeneous carbonaceous materials by Raman spectroscopy. *Spectrochimica Acta Part A: Molecular and Biomolecular Spectroscopy* 59, 2267–2276. doi:10.1016/S1386-1425(03)00070-2
- Bouchez, J., Beyssac, O., Galy, V., Gaillardet, J., France-Lanord, C., Maurice, L., Moreira-Turcq, P., 2010. Oxidation of petrogenic organic carbon in the Amazon floodplain as a source of atmospheric CO₂. *Geology* 38, 255–258. doi:10.1130/G30608.1
- Buseck, P.R., Beyssac, O., 2014. From Organic Matter to Graphite: Graphitization. *Elements* 10, 421–426. doi:10.2113/gselements.10.6.421
- Cartwright, I., Buick, I.S., 2000. Fluid generation, vein formation and the degree of fluid–rock interaction during decompression of high- pressure terranes: the Schistes Lustrés, Alpine Corsica, France. *Journal of metamorphic Geology* 18, 607–624. doi:10.1046/j.1525-1314.2000.00280.x
- Cesare, B., 1995. Graphite precipitation in C-O-H fluid inclusions: closed system compositional density changes, and thermobarometric implications. *Contributions to Mineralogy and Petrology* 122, 25–33.
- Connolly, J.A.D., 1995. Phase diagram methods for graphitic rocks and application to the system C–O–H–FeO–TiO₂–SiO₂. *Contributions to Mineralogy and Petrology* 119, 94–116.
- Connolly, J.A.D., Cesare, B., 1993. C- O- H- S fluid composition and oxygen fugacity in graphitic metapelites. *Journal of metamorphic Geology* 11, 379–388.
- Cook-Kollars, J., Bebout, G.E., Collins, N.C., Angiboust, S., Agard, P., 2014. Subduction zone metamorphic pathway for deep carbon cycling: I. Evidence from HP/UHP metasedimentary rocks, Italian Alps. *Chemical Geology* 386, 31–48. doi:10.1016/j.chemgeo.2014.07.013
- Duke, E.F., Rumble, D., 1986. Textural and isotopic variations in graphite from plutonic rocks, South-Central New Hampshire. *Contributions to Mineralogy and Petrology* 93, 409–419. doi:10.1007/BF00371711
- Duncan, M.S., Dasgupta, R., 2017. Rise of Earth’s atmospheric oxygen controlled by efficient subduction of organic carbon. *Nature Geoscience* 10, 387–392. doi:10.1038/ngeo2939
- Elter, G., 1971. Schistes lustrés et ophiolites de la zone piémontaise entre Orco et Doire Baltée (Alpes Graies). Hypothèses sur l'origine des ophiolites. *Géologie Alpine* 47, 147–169.
- Evans, K.A., Bickle, M.J., Skelton, A.D.L., Hall, M., Chapman, H., 2002. Reductive deposition of graphite at lithological margins in East Central Vermont: a Sr, C and O

- isotope study. *Journal of metamorphic Geology* 20, 781–798. doi:10.1046/j.1525-1314.2002.00403.x
- Facq, S.B., Daniel, I., Montagnac, G., Cardon, H., Sverjensky, D.A., 2014. In situ Raman study and thermodynamic model of aqueous carbonate speciation in equilibrium with aragonite under subduction zone conditions. *Geochimica et Cosmochimica Acta* 132, 375–390. doi:10.1016/j.gca.2014.01.030
- Fournier, M., Jolivet, L., Goff, B., Dubois, R., 1991. Alpine Corsica metamorphic core complex. *Tectonics* 10, 1173–1186.
- Gabalda, S., Beyssac, O., Jolivet, L., Agard, P., Chopin, C., 2009. Thermal structure of a fossil subduction wedge in the Western Alps. *Terra Nova* 21, 28–34. doi:10.1111/j.1365-3121.2008.00849.x
- Galvez, M.E., Beyssac, O., Martinez, I., Benzerara, K., Chaduteau, C., Malvoisin, B., Malavieille, J., 2013. Graphite formation by carbonate reduction during subduction. *Nature Geoscience* 6, 473–477. doi:10.1038/ngeo1827
- Galy, V., Beyssac, O., France-Lanord, C., Eglinton, T., 2008. Recycling of graphite during Himalayan erosion: A geological stabilization of carbon in the crust. *Science* 322, 943–945.
- Gorman, P.J., Kerrick, D.M., Connolly, J.A.D., 2006. Modeling open system metamorphic decarbonation of subducting slabs. *Geochemistry, Geophysics, Geosystems* 7, 1–21. doi:10.1029/2005GC001125
- Groppo, C., Castelli, D., 2010. Prograde P–T Evolution of a Lawsonite Eclogite from the Monviso Meta-ophiolite (Western Alps): Dehydration and Redox Reactions during Subduction of Oceanic FeTi-oxide Gabbro. *Journal of Petrology* 51, 2489–2514. doi:10.1093/petrology/egq065
- Hayes, J.M., Waldbauer, J.R., 2006. The carbon cycle and associated redox processes through time. *Philosophical Transactions of the Royal Society B: Biological Sciences* 361, 931–950. doi:10.1098/rstb.2006.1840
- Hermann, J., Spandler, C., Hack, A., Korsakov, A., 2006. Aqueous fluids and hydrous melts in high-pressure and ultra-high pressure rocks: Implications for element transfer in subduction zones. *Lithos* 92, 399–417. doi:10.1016/j.lithos.2006.03.055
- Holloway, J.R., 1984. Graphite-CH₄-H₂O-CO₂ equilibria at low-grade metamorphic conditions. *Geology* 12, 455–458.
- Kelemen, P.B., Manning, C.E., 2015. Reevaluating carbon fluxes in subduction zones, what goes down, mostly comes up. *PNAS* 112, E3997–E4006. doi:10.1073/pnas.1507889112
- Lagabrielle, Y., Lemoine, M., 1997. Alpine, Corsican and Apennine ophiolites: the slow-spreading ridge model. *Comptes Rendus de l'Académie des Sciences* 325, 909–920.
- Lagabrielle, Y., Vitale Brovarone, A., Ildefonse, B., 2015. Fossil oceanic core complexes recognized in the blueschist metaophiolites of Western Alps and Corsica. *Earth Science Reviews* 141, 1–26. doi:10.1016/j.earscirev.2014.11.004
- Lemoine, M., 2003. Schistes lustrés from Corsica to Hungary : back to the original sediments and tentative dating of partly azoic metasediments 174, 197–209.
- Luque, F.J., Ortega, L., Barrenechea, J.F., Millward, D., Beyssac, O., Huizenga, J.-M., 2009. Deposition of highly crystalline graphite from moderate-temperature fluids. *Geology* 37, 275–278. doi:10.1130/G25284A.1
- Mori, Y., Shigeno, M., Nishiyama, T., 2014. Fluid-metapelite interaction in an ultramafic mélange: implications for mass transfer along the slab-mantle interface in subduction zones 66, 1–8. doi:10.1186/1880-5981-66-47
- Mullis, J., Dubessy, J., Poty, B., O'Neil, J., 1994. Fluid regimes during late stages of a continental collision: Physical, chemical, and stable isotope measurements of fluid inclusions in fissure quartz from a geotraverse through the Central Alps, Switzerland. *Chemical Geology* 58, 2239–2267. doi:10.1016/0016-7037(94)90008-6
- Newton, R.C., Manning, C.E., 2009. Hydration state and activity of aqueous silica in H₂O-CO₂ fluids at high pressure and temperature. *American Mineralogist* 94, 1287–1290. doi:10.2138/am.2009.3287

- Nitsch, K.-H., 1972. Das P-T-X_{CO2} Stabilitätsfeld von Lawsonit. *Contributions to Mineralogy and Petrology* 34, 116–134.
- Pattison, D.R.M., 2006. The fate of graphite in prograde metamorphism of pelites: An example from the Ballachulish aureole, Scotland. *Lithos* 88, 85–99. doi:10.1016/j.lithos.2005.08.006
- Piccoli, F., Hermann, J., Pettke, T., Connolly, J.A.D., Kempf, E.D., Duarte, J.F.V., 2019. Subducting serpentinites release reduced, not oxidized, aqueous fluids. *Scientific Reports* 9, 1–7. doi:10.1038/s41598-019-55944-8
- Piccoli, F., Vitale Brovarone, A., Beyssac, O., Martinez, I., Ague, J.J., Chaduteau, C., 2016. Carbonation by fluid–rock interactions at high-pressure conditions: Implications for carbon cycling in subduction zones. *Earth and Planetary Science Letters* 445, 146–159. doi:10.1016/j.epsl.2016.03.045
- Plank, T., 2014. 4.17 The Chemical Composition of Subducting Sediments, 2nd ed, The Crust. Elsevier Ltd. doi:10.1016/B978-0-08-095975-7.00319-3
- Poli, S., 2015. Carbon mobilized at shallow depths in subduction zones by carbonatitic liquids. *Nature Geoscience* 8, 633–636. doi:10.1038/ngeo2464
- Polino, R., Lemoine, M., 1984. Détritisme mixte d'origine continentale et océanique dans les sédiments jurassico-crétacés supra-ophiolitiques de la Téthys Ligure: la série du Lago Nero (Alpes Occidentales franco-italiennes). *Comptes Rendus de l'Académie des Sciences* 298, 359–364.
- Ravna, E.J.K., Andersen, T.B., Jolivet, L., de Capitani, C., 2010. Cold subduction and the formation of lawsonite eclogite - constraints from prograde evolution of eclogitized pillow lava from Corsica 28, 381–395. doi:10.1111/j.1525-1314.2010.00870.x
- Schwartz, S., Guillot, S., Reynard, B., Lafay, R., Debret, B., Nicollet, C., Lanari, P., Auzende, A.L., 2013. Pressure–temperature estimates of the lizardite/antigorite transition in high pressure serpentinites. *Lithos* 178, 197–210. doi:10.1016/j.lithos.2012.11.023
- Souche, A., Beyssac, O., Andersen, T.B., 2012. Thermal structure of supra-detachment basins: a case study of the Devonian basins of western Norway. *Journal of the Geological Society* 169, 427–434. doi:10.1144/0016-76492011-155
- Tarantola, A., Mullis, J., Vennemann, T., Chemical, J.D., de Capitani, C., 2007. Oxidation of methane at the CH₄/H₂O–(CO₂) transition zone in the external part of the Central Alps, Switzerland: evidence from stable isotope investigations. *Chemical Geology* 237, 329–357. doi:10.1016/j.chemgeo.2006.07.007
- Tiraboschi, C., 2018. Experimental determination of magnesia and silica solubilities in graphite-saturated and redox-buffered high-pressure COH fluids in equilibrium with forsterite + enstatite and magnesite + enstatite. *Contributions to Mineralogy and Petrology* 173, 1–17. doi:10.1007/s00410-017-1427-0
- Tumiati, S., Malaspina, N., 2019. Redox processes and the role of carbon-bearing volatiles from the slab–mantle interface to the mantle wedge. *Journal of the Geological Society* 176, 388–397. doi:10.1144/jgs2018-046
- Tumiati, S., Tiraboschi, C., Miozzi, F., Vitale Brovarone, A., Manning, C.E., Sverjensky, D.A., Milani, S., Poli, S., 2020. Dissolution susceptibility of glass-like carbon versus crystalline graphite in high-pressure aqueous fluids and implications for the behavior of organic matter in subduction zones. *Geochimica et Cosmochimica Acta* 273, 383–402. doi:10.1016/j.gca.2020.01.030
- Tumiati, S., Tiraboschi, C., Sverjensky, D.A., Pettke, T., Recchia, S., Ulmer, P., Miozzi, F., Poli, S., 2017. Silicate dissolution boosts the CO₂ concentrations in subduction fluids. *Nature Communications* 1–11. doi:10.1038/s41467-017-00562-z
- Vitale Brovarone, A., Agard, P., Monié, P., Chauvet, A., Rabaute, A., 2018a. Tectonic and metamorphic architecture of the HP belt of New Caledonia. *Earth Science Reviews* 178, 48–67. doi:10.1016/j.earscirev.2018.01.006
- Vitale Brovarone, A., Alard, O., Beyssac, O., Martin, L., Picatto, M., 2014a. Lawsonite metasomatism and trace element recycling in subduction zones. *Journal of metamorphic Geology* 32, 489–514. doi:10.1111/jmg.12074

- Vitale Brovarone, A., Beyssac, O., 2014. Lawsonite metasomatism: A new route for water to the deep Earth. *Earth and Planetary Science Letters* 393, 275–284. doi:10.1016/j.epsl.2014.03.001
- Vitale Brovarone, A., Beyssac, O., Malavieille, J., Molli, G., Beltrando, M., Compagnoni, R., 2013. Stacking and metamorphism of continuous segments of subducted lithosphere in a high-pressure wedge: The example of Alpine Corsica (France). *Earth Science Reviews* 116, 35–56. doi:10.1016/j.earscirev.2012.10.003
- Vitale Brovarone, A., Chu, X., Martin, L.A.J., Ague, J.J., Monié, P., Groppo, C., Martinez, I., Chaduteau, C., 2018b. Intra-slab COH fluid fluxes evidenced by fluid-mediated decarbonation of lawsonite eclogite-facies altered oceanic metabasalts. *Lithos* 304–307, 211–229. doi:10.1016/j.lithos.2018.01.028
- Vitale Brovarone, A., Martinez, I., Elmaleh, A., Compagnoni, R., Chaduteau, C., Ferraris, C., Esteve, I., 2017. Massive production of abiotic methane during subduction evidenced in metamorphosed ophicarbonates from the Italian Alps. *Nature Communications* 8, 14134–13. doi:10.1038/ncomms14134
- Vitale Brovarone, A., Picatto, M., Beyssac, O., Lagabrielle, Y., Castelli, D., 2014b. The blueschist–eclogite transition in the Alpine chain: P–T paths and the role of slow-spreading extensional structures in the evolution of HP–LT mountain belts. *Tectonophysics* 615–616, 96–121. doi:10.1016/j.tecto.2014.01.001
- Wilson, C.R., Spiegelman, M., van Keken, P.E., Hacker, B.R., 2014. Fluid flow in subduction zones: The role of solid rheology and compaction pressure. *Earth and Planetary Science Letters* 401, 261–274. doi:10.1016/j.epsl.2014.05.052
- Zhang, S., Ague, J.J., Brovarone, A.V., 2018. Degassing of organic carbon during regional metamorphism of pelites, Wepawaug Schist, Connecticut, USA. *Chemical Geology* 490, 30–44. doi:10.1016/j.chemgeo.2018.05.003
- Ziegenbein, D., Johannes, W., 1980. Graphite in C-H-O fluids: unsuitable compound to buffer fluid composition at temperatures up to 700°C. *Neues Jahrbuch Mineralogie Monatshefte* 7, 289–305.

Figure Captions

Figure 1

Metamorphic maps of the study areas in Alpine Corsica (a) and Western Alps (b), modified after Vitale Brovarone, Picatto et al. (2014) and Schwartz et al., (2013), respectively. Estimated peak conditions based on Raman Spectroscopy of Carbonaceous Material and thermodynamics are also shown. In Alpine Corsica, the lower-grade T appearance of CM leaching in metasomatic aureoles corresponds to the field-based isograd for lawsonite metasomatism (~ 370 °C), while in the Western Alps, similar processes were found at lower T in the range of 330–340 °C.

Figure 2

(a-c) Examples of lawsonite-bearing, CM depleted reaction zones in contact with mafic/ultramafic blocks in Alpine Corsica (See also Fig. 5 for a detailed profile). (a-a') Example of a relatively thin reaction zone in contact with a small metagabbro block. The bleaching zone next to the contact (red line) is highlighted in (a'), which also show the

distribution of CM-rich lawsonite blasts (small, elongated rectangles). The size of the blasts in not to scale). (b-c) Close-up and photomicrograph of the CM-depleted zone marked by the red box in (a'). In (c), note the presence of a CM-rich foliation preserved in the lawsonite blasts. (d-f) Example of lawsonite-bearing, CM-depleted individual layers within the metasedimentary suite in the absence of mafic/ultramafic blocks (d-f). In (f), note the presence of CM-rich lawsonite crystals preserved in a CM-poor matrix.

Figure 3

Examples of lawsonite-bearing, CM-depleted reaction zones in contact with mafic/ultramafic rocks in the Western Alps. (a-d) General distribution and patterns of CM-leaching and lawsonite precipitation (bleached area in a') around metabasaltic blocks (green blocks in (a')). The size of the lawsonite blasts (small, elongated rectangles in (a')) is not to scale. (b-d) Close-ups and photomicrograph of the CM-depleted zone marked by the red box in (a'). In (d), note the presence of a CM-rich foliation preserved in the lawsonite blasts. (e-h) General distribution and patterns of CM-leaching and lawsonite precipitation (bleached area in e') in a complexly deformed calcschist + metachert sequence in contact with an ultramafic block (green zone in (e')). The size of the lawsonite blasts (small, elongated rectangles in (e')) is not to scale and is confined to the calcschist layers initially present in the rock. (f-h) Close-ups and photomicrograph of the CM-depleted zone marked by the red box in (e'). In (g-h), note the presence of a CM-rich foliation preserved in the lawsonite blasts in a chlorite-lawsonite rich (g) and a quartz-carbonate-mica (h) layer.

Figure 4

Microstructural features of lawsonite-rich metasomatic rocks showing evidence for fluid-mediated CM dissolution in both Alpine Corsica (a-c) and Western Alps (d-f) blueschist-facies units. (b,d) are from metasomatic aureoles surrounding ultramafic block, whereas all others surround metagabbro blocks. Note the abundance of CM (\pm rutile needles) included in lawsonite. Note also, in (a-b), the presence of a CM-free rim in the lawsonite crystals. The T estimates for each panel are from Vitale Brovarone et al. (2014b) and Schwartz et al., (2013).

Figure 5

Field image and characteristic microstructural features of the selected metasomatic aureole. The outcrop exposes the contact (red line) between a metagabbro block (right) and the embedding metasedimentary rocks. The metasediment shows a progressive compositional and mineralogical variation towards the contact zone leading to an intense bleaching of the rock. Z1(least altered or not altered): phengite(\sim 45vol%), chlorite(40%), quartz(10), accessory

phases(5%); Z2: phengite(30%), chlorite(35%), quartz(15%), lawsonite(15%), accessory
phases(5%); Z3: phengite(25%), chlorite(25%), quartz(30%), lawsonite(15%), accessory
phases(5%); Z4: phengite(15%), chlorite(15%), quartz(50%), albite(10%), lawsonite(5%)
accessory phases(5%); Z5: albite(40%), blue-amphibole(30%), chlorite(20%), quartz(5%),
accessory phases(5%). Photomicrographs are reported for each zone of the least to the most
altered pelitic schist (bottom).

Figure 6

Whole-rock C content across the reaction zone shown in Figure 5. Note the progressive
decrease in organic C, present as CM in the studied samples, towards the contact zone, and
the main drops at the Z2-Z3 and Z3-Z4 boundaries. Note that only one sample (sample 2f)
contain little C other than organic C (0.5 wt%) and interpreted as carbonate. For each zone,
the average distance from the metagabbro is indicated. The “0” value corresponds to the
interface between the metagabbro and the metapelite.

Figure 7

(a-c) Representative Raman spectra of CM in the studies samples and corresponding R2
values. The defect bands (D1-D2) and the associated R2 values decrease from (a) to (c).
Rather crystalline graphite in (c) has very small D1-D2 bands. See Figure 8 for a complete
Raman characterization of CM from Z1 to Z5. Spectrum (a) is characteristic of the dominant
CM cluster in samples unaffected by fluid-mediated transformations and of the CM preserved
as inclusions in fluid-precipitated minerals such as lawsonite. Spectra (b) and (c) are
representative of the dominant CM cluster in the matrix of samples characterized by intense
fluid-mediated transformations, and is also present as minor cluster in the protolith metapelite
unaffected by metasomatism. Examples of microstructural distribution of different types of
CM in the studies samples are shown (d-e), with higher R2 CM preserved as inclusions in
lawsonite, and lower R2 CM preserved in the rock matrix. See Figure 8 and Table 2 for
distribution of R2 values across the selected reaction zone.

Figure 8

Results of RSCM and characteristic photomicrographs for the different reaction zones. Z1:
least altered metapelite including dark, CM-rich titanite (Ttn); Z2: lawsonite-bearing
metapelite. Note the precipitation of lawsonite in the CM-rich metapelite; Z3: lawsonite-
bearing schist. Here, dark, CM-rich lawsonite (same as Z2) floats in a bleached, CM-poor
matrix; Z4: quartz-albite schist preserving relicts of CM-rich lawsonite; Blue-amphibole-
chlorite schist. Rare relicts of CM are present as inclusions in titanite. The histograms to the

right show the structural variation of CM throughout the reaction zone based on Raman analysis, expressed as R2 (relative area of the defect band of CM in Raman spectra Section 4.2). CM_{inc} in lawsonite and titanite shows constant R2 values throughout the reaction zone, except for the more internal zone where it shows a much lower R2. CM_m is similar to CM_{inc} in Z1, whereas it shifts towards lower R2 values approaching the contact zone. In Z5, any CM was found in the matrix.

Figure 9

Concentration ratio diagram for fluid-mobile element profiles across the interaction zone.

Note the depletion in K, Ba, Rb and Cs on both sides of the contact zone suggesting a dominantly advective mechanism of mass transport.

Figure 10

Estimated time-integrated fluid fluxes required to mobilize the calculated CM loss from each reaction zone. For each P-T condition, results for both glass-like C (lower bounds) and crystalline graphite (upper bounds) are shown. The more disorder CM cluster in the selected samples is expected to lie in between. The values on the vertical axis are dependent on the parameter n, which is the Log of L (distance of the reaction front). See Figure 11 for graphical examples.

Figure 11

Schematic representation of the distribution and magnitude of channelized fluid flow within the blueschist-facies, block-in-matrix units of Alpine Corsica and Western Alps. Values of time-integrated fluid flux (in m³/m²) refer to the minimum fluxes required to mobilize CM at P ranging from ~1 to ~2 GPa and T ranging from 300 to about 450 °C. L = distance of reaction front propagation.

Table Captions

Table 1. Bulk organic C and total CO₂ content in the selected samples across the metasomatic aureole.

Table 2. RSCM R2 values of matrix and inclusion CM throughout the studied reaction zone.

Table 3. Calculated fractional mass change and organic C loss per 100g of rock for Zr, Hf, and Th.

Table 4. Fluid component speciation considered for mass balances and flux estimates, calculated by thermodynamic modelling of COH fluids saturated with graphite and glass-like carbon.

Table 5. Calculated time-integrated fluid fluxes at H₂O-maximum. For each sample, q_{TI} is calculated by considering the CM fractional change relative to the average of Z1.

Figure 1

Map of the Mediterranean region showing the location of the study area. The map includes the Alps, the Balearic Islands, and the Mediterranean Sea. A scale bar indicates 250 Km. Latitude lines for 40°N and 45°N are shown. Longitude lines for 5°, 10°, and 15° are shown. A north arrow is present. Two red boxes labeled 'Fig. 1a' and 'Fig. 1b' are placed on the map, indicating the locations of the study areas.

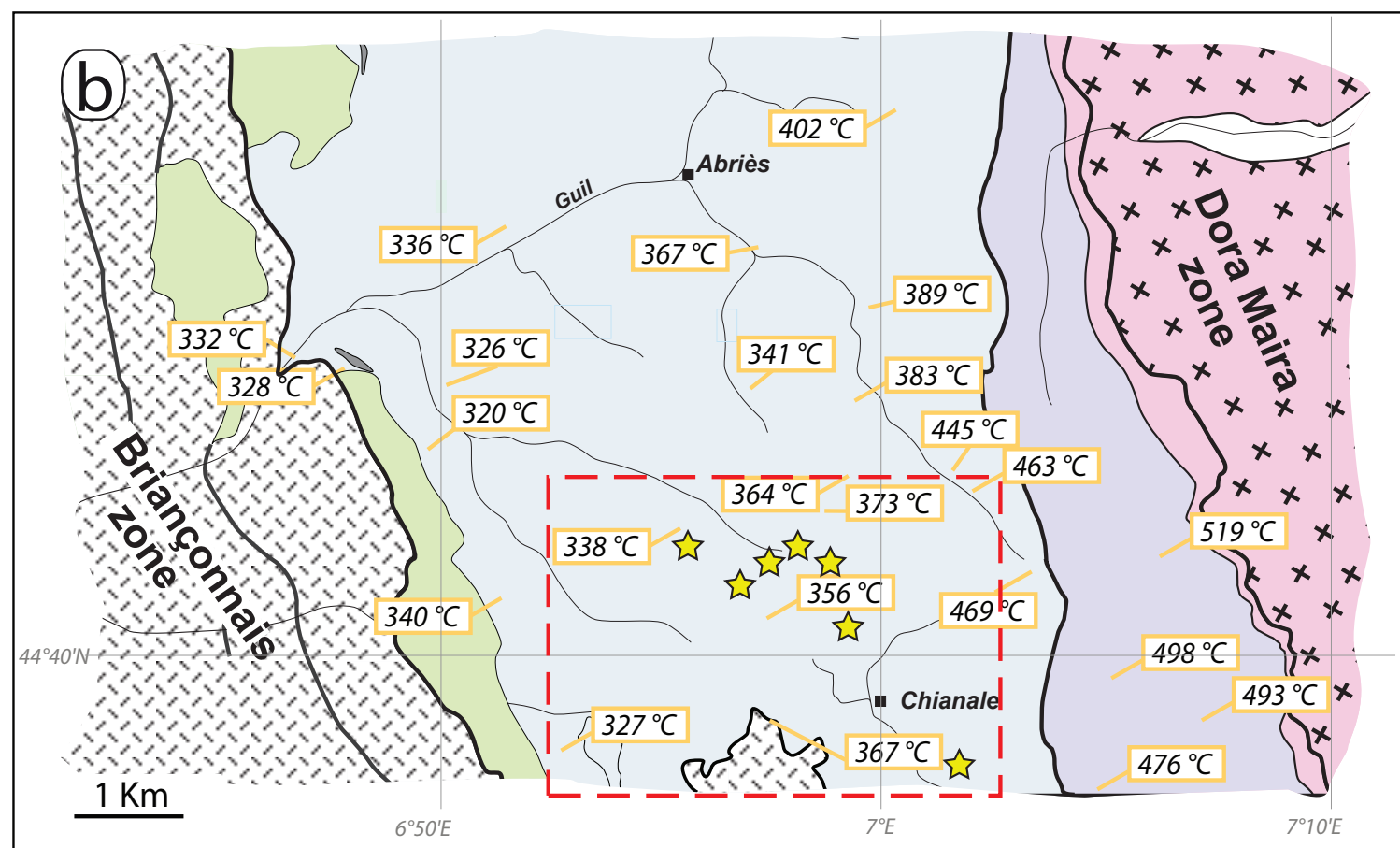
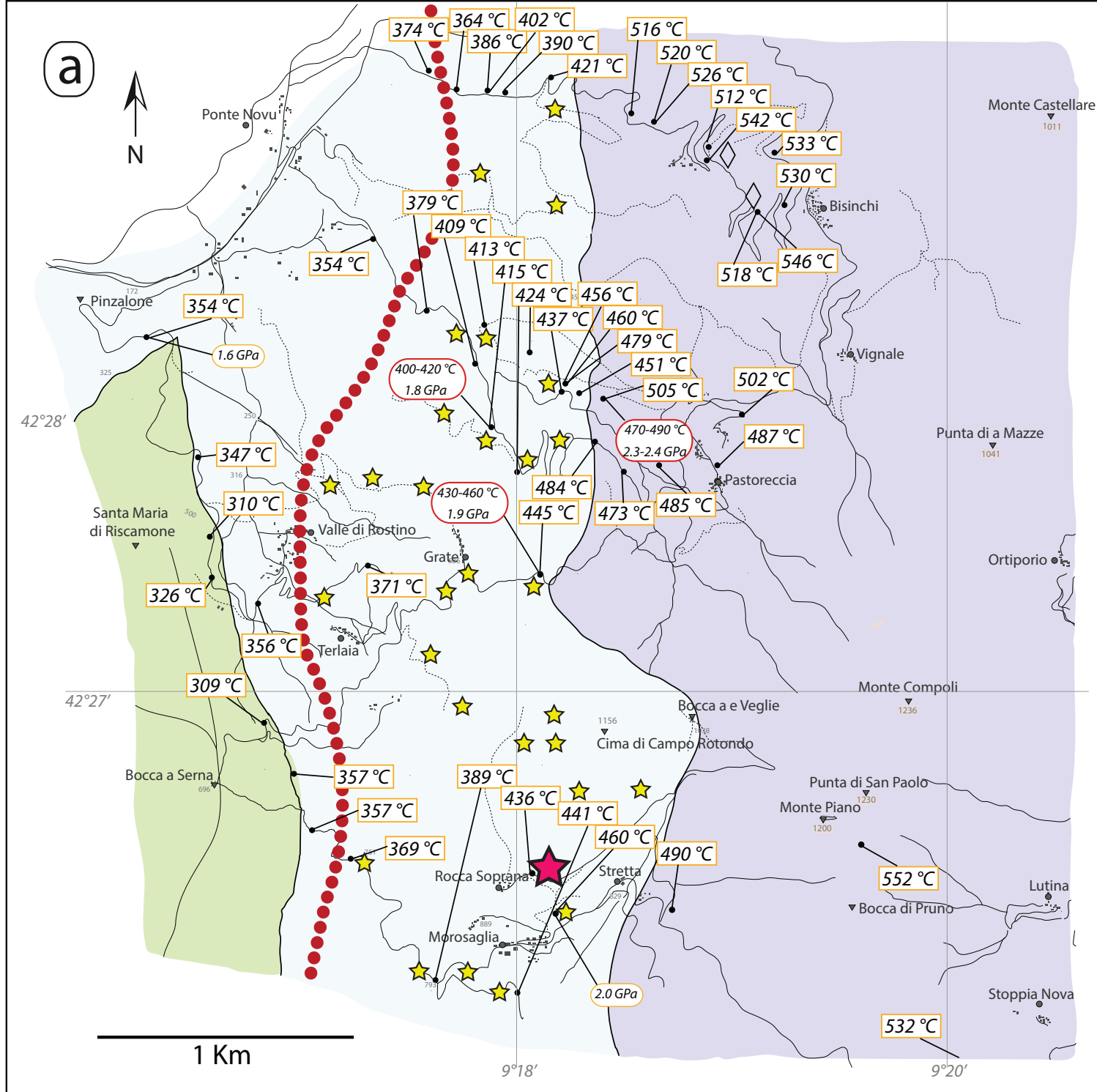
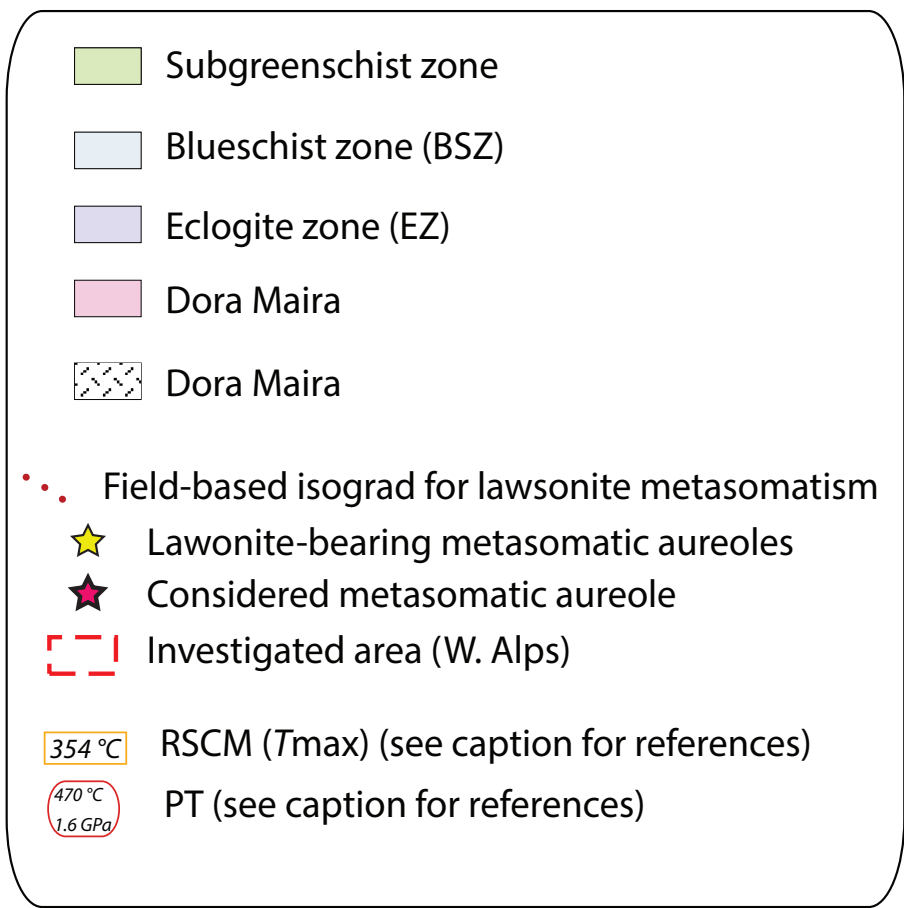
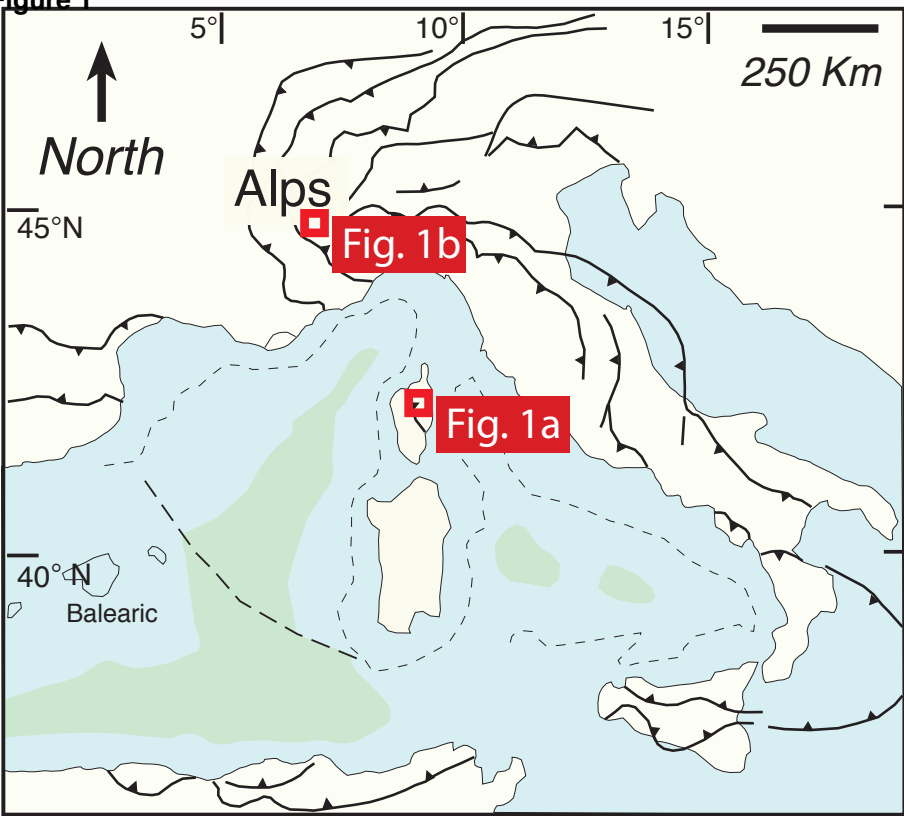


Figure 2
[Click here to download high resolution image](#)

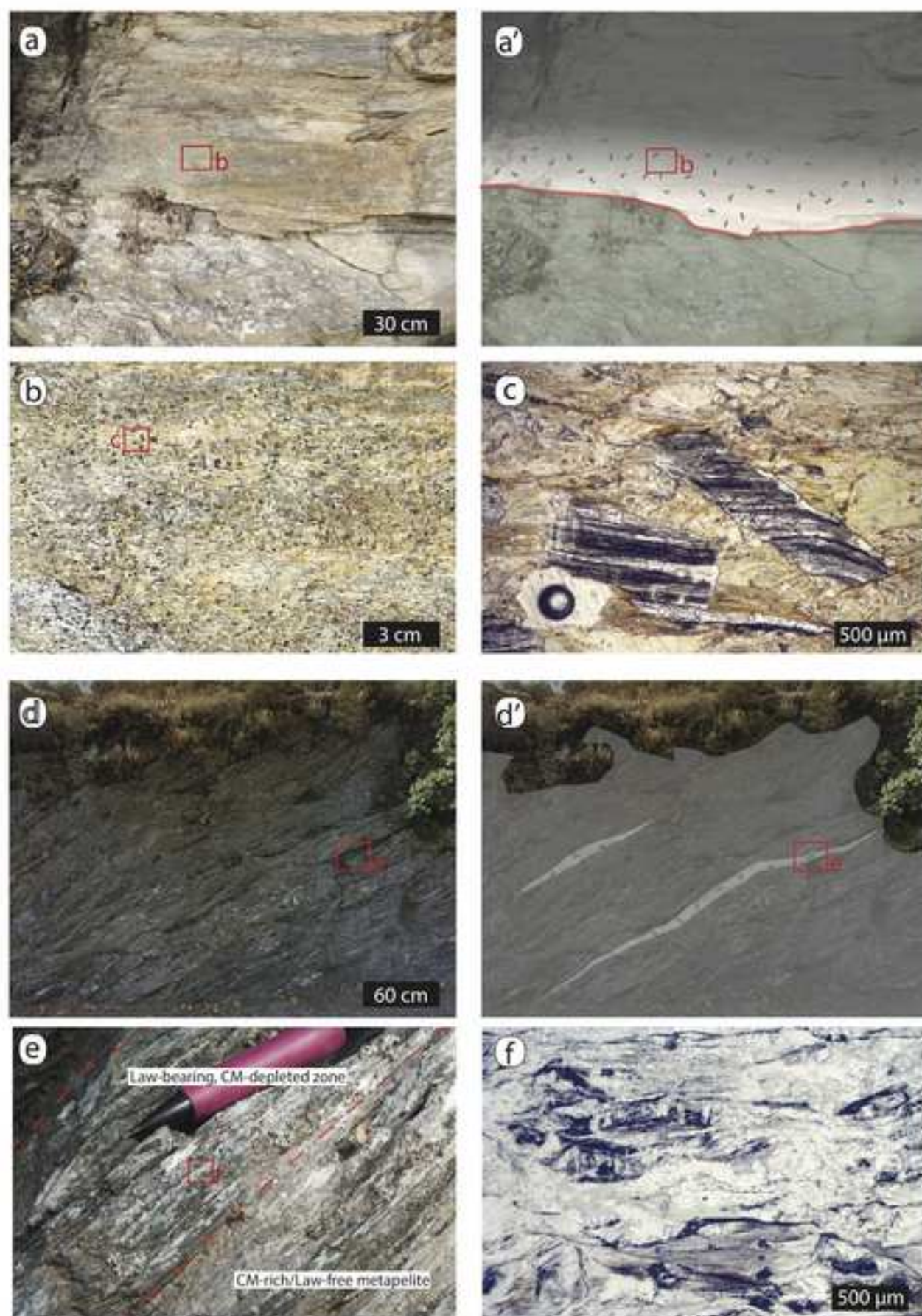


Figure 3
[Click here to download high resolution image](#)

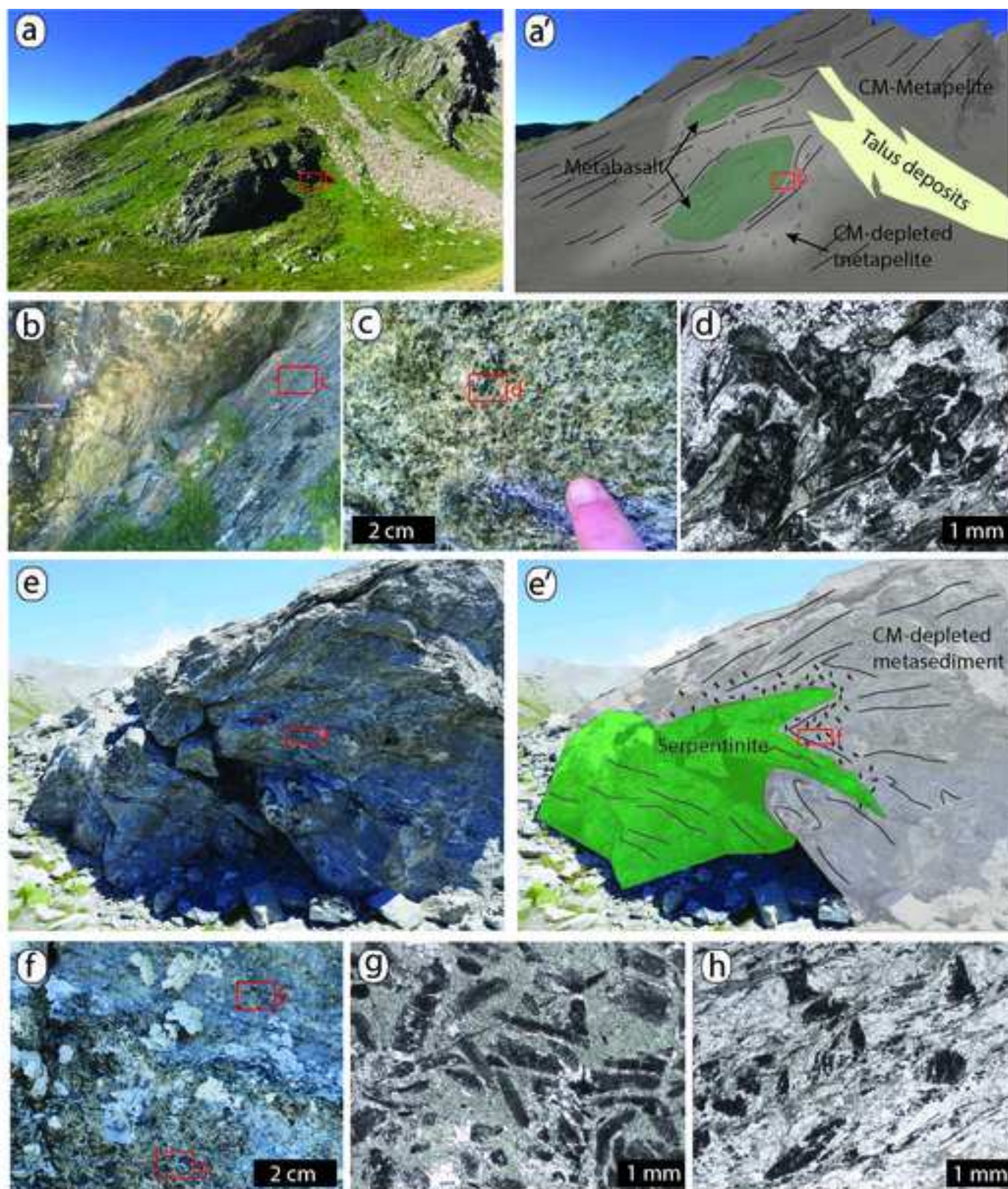


Figure 4
[Click here to download high resolution image](#)

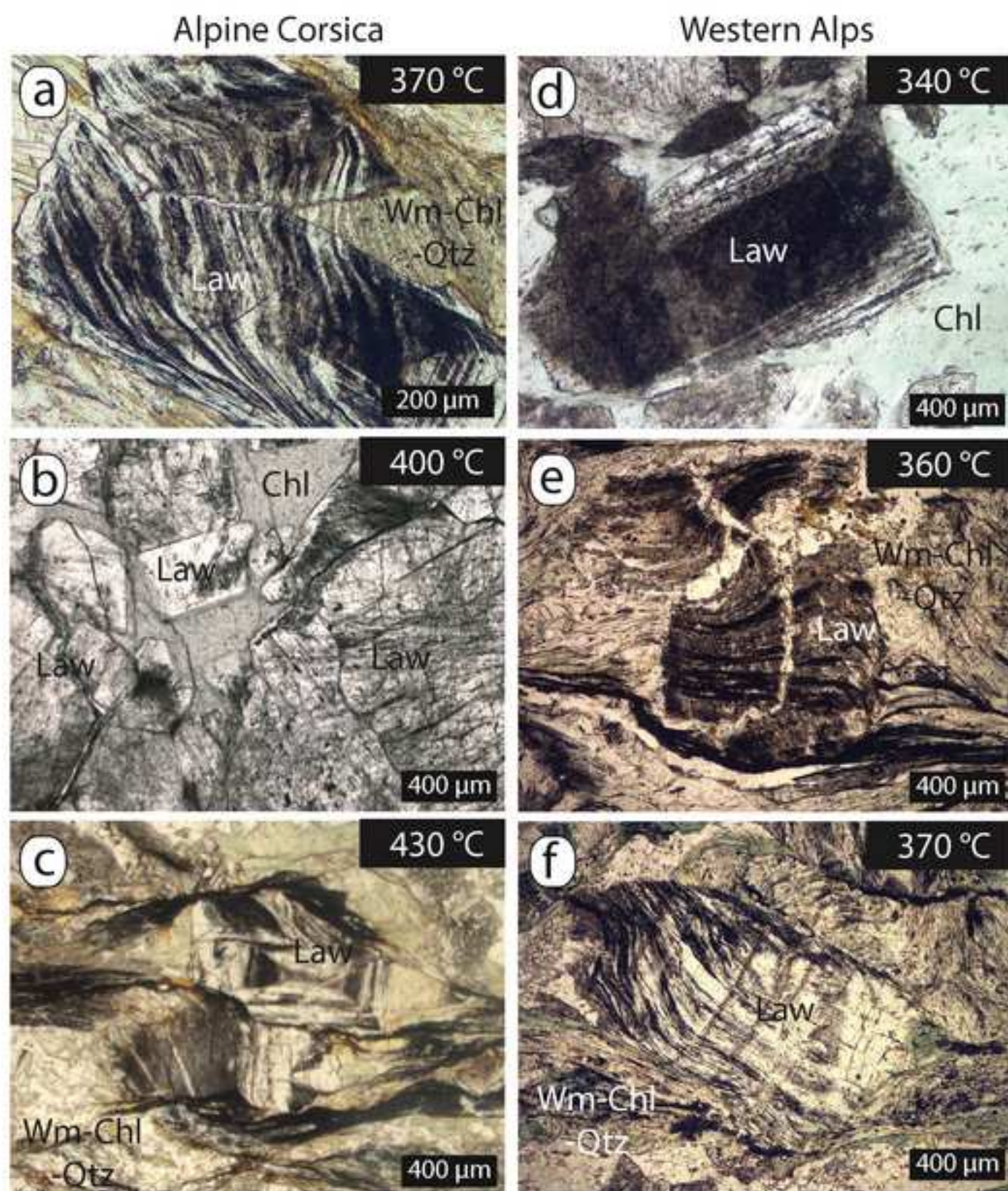


Figure 5
[Click here to download high resolution image](#)

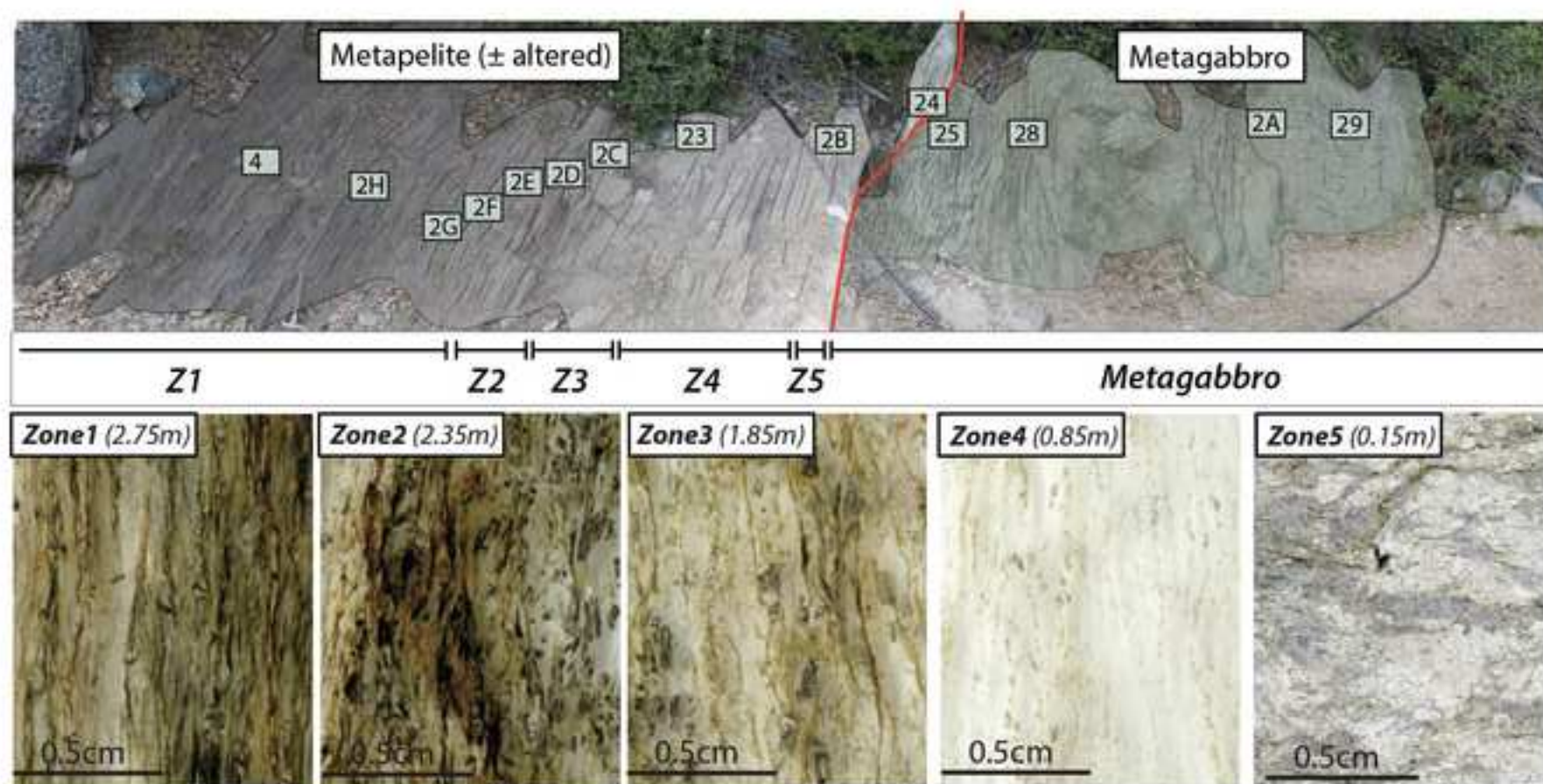


Figure 6

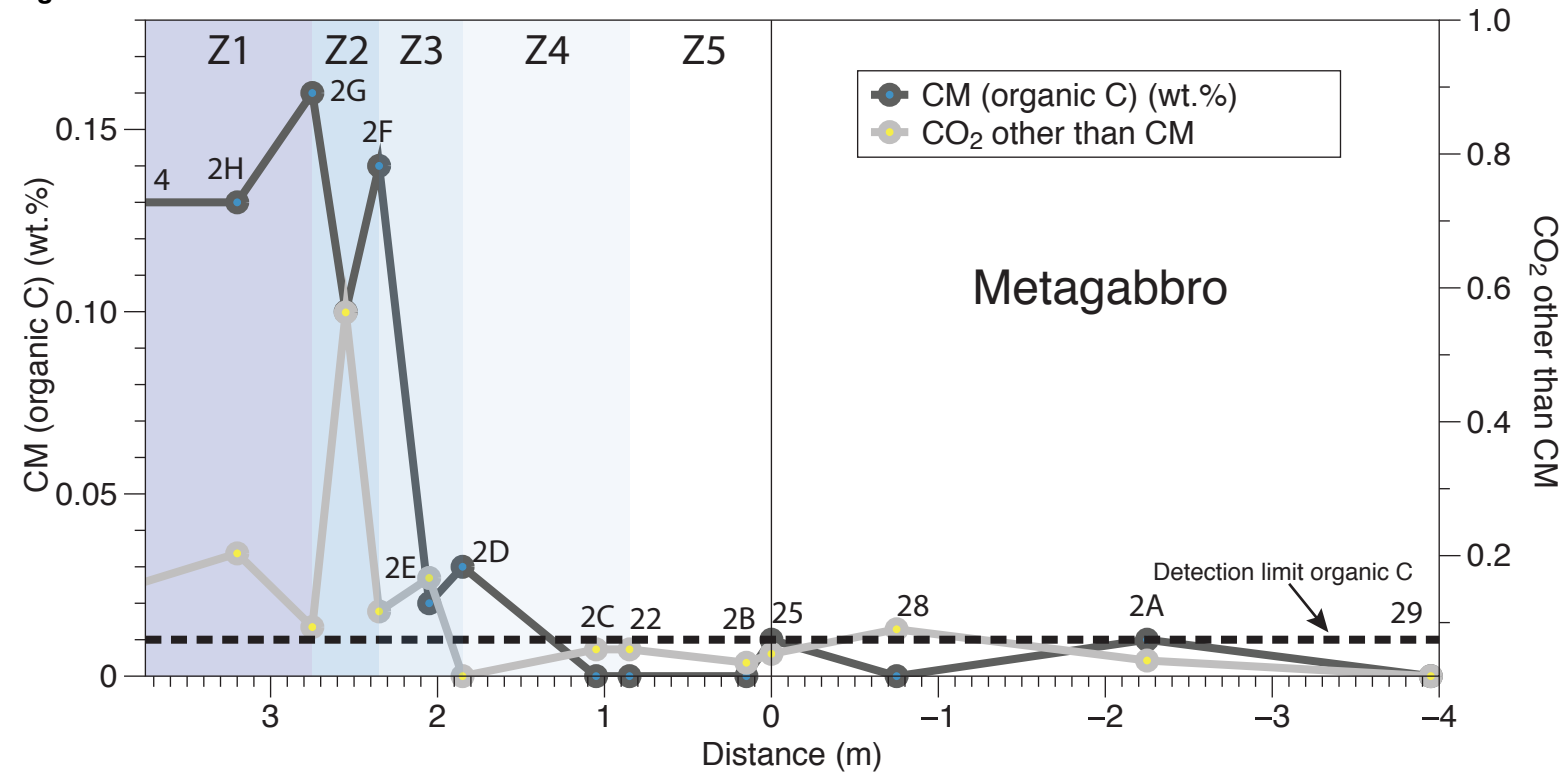


Figure 7
[Click here to download high resolution image](#)

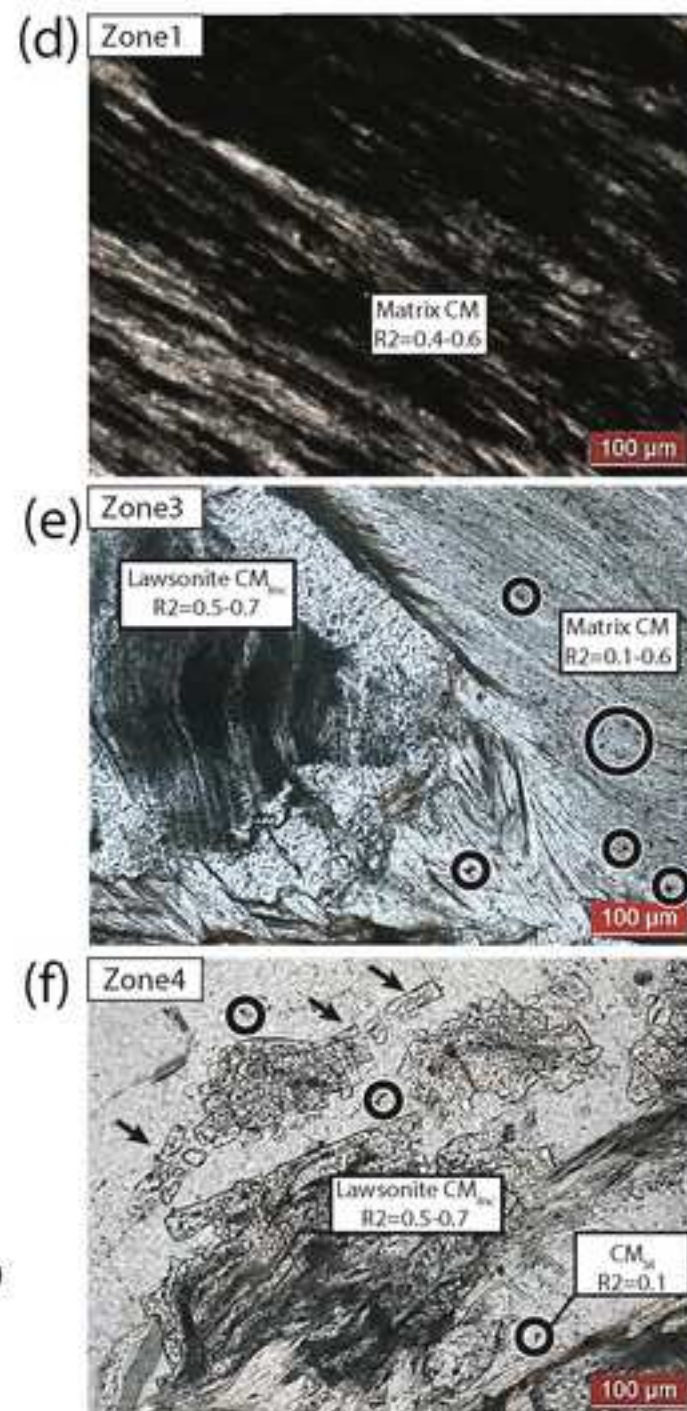
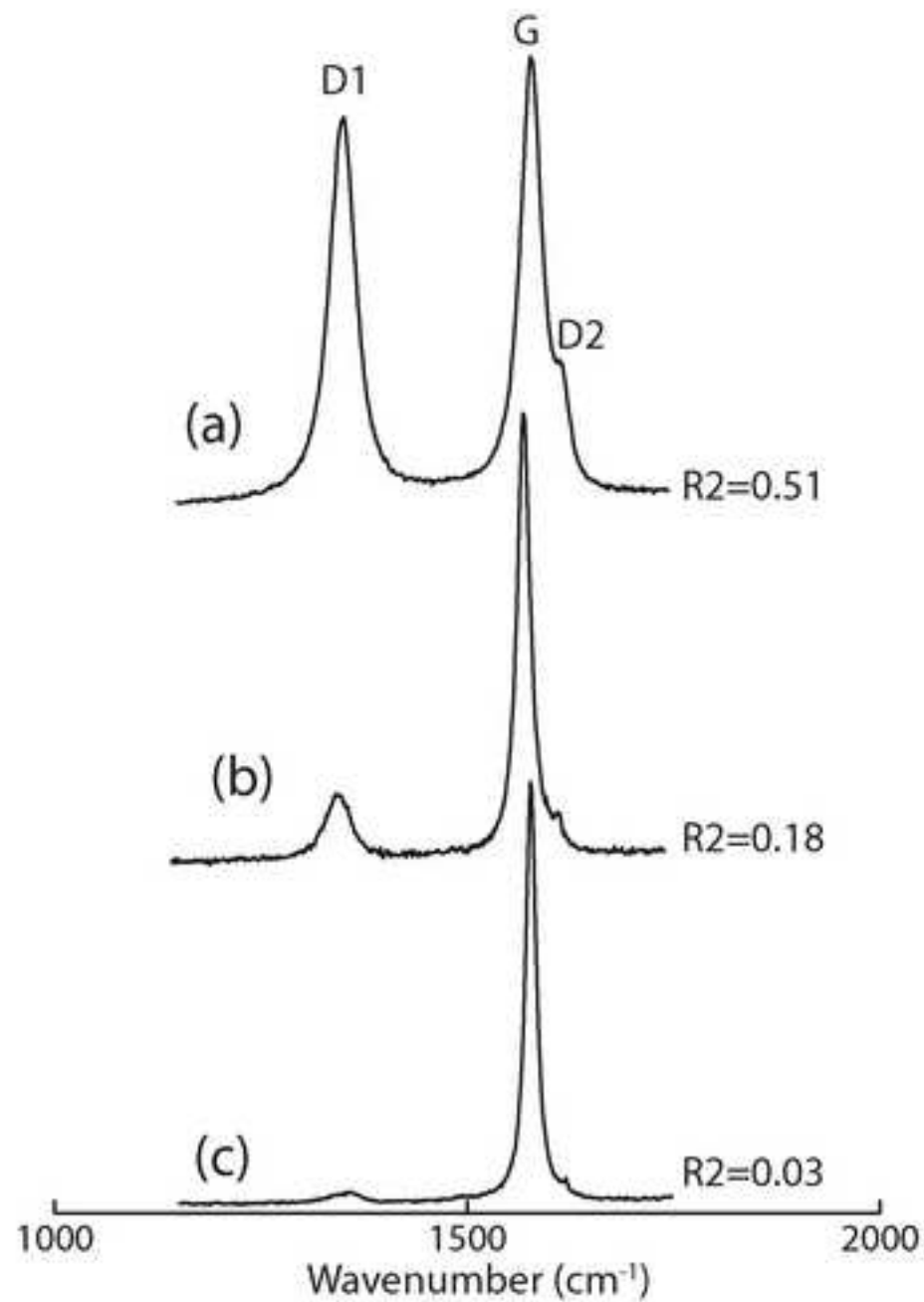


Figure 8

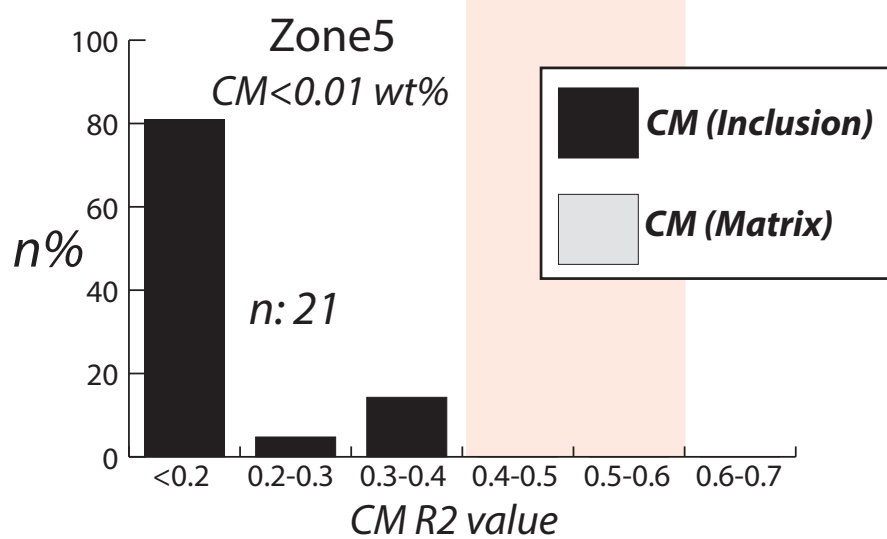
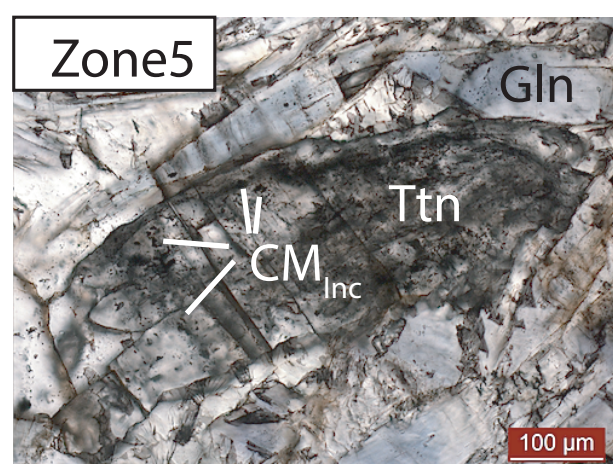
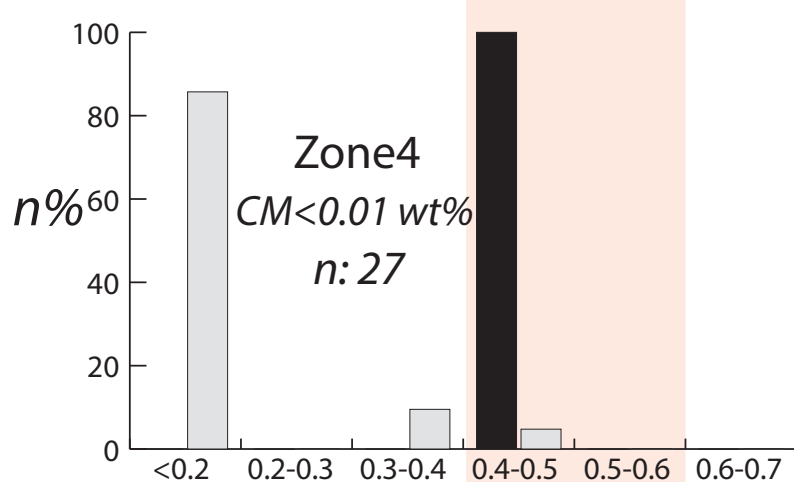
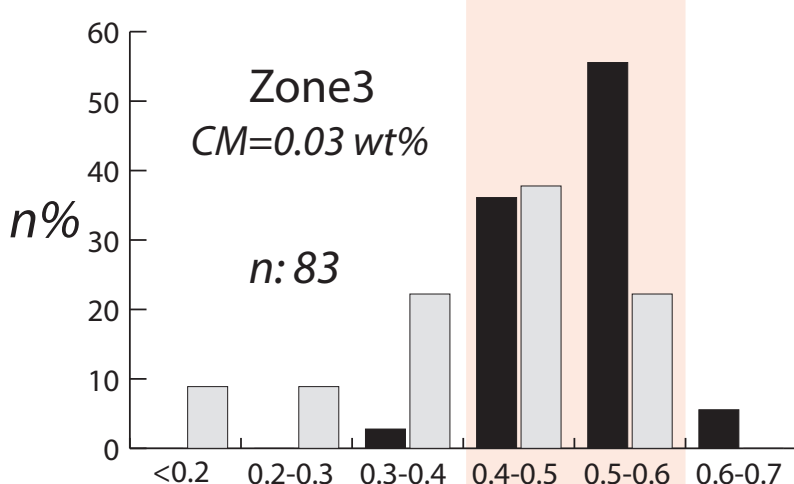
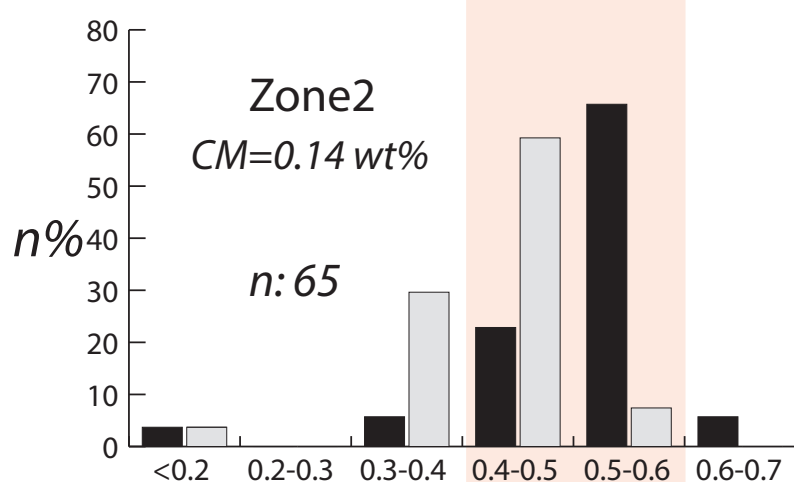
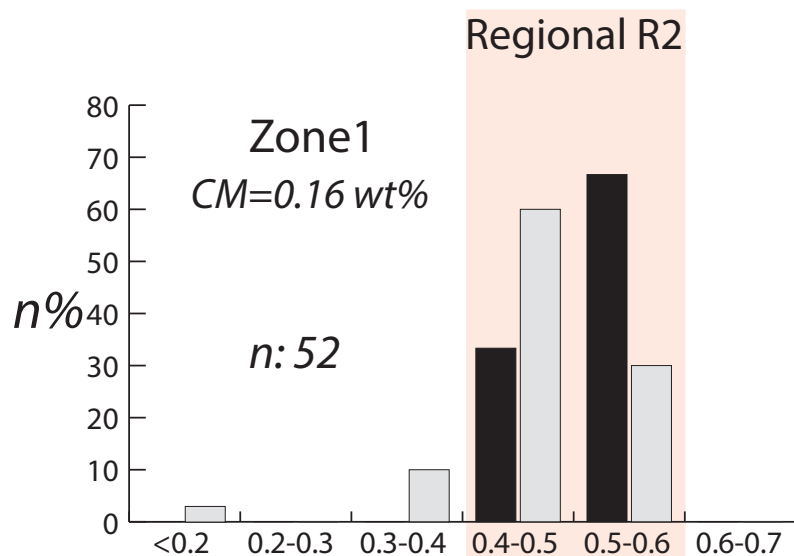


Figure 9

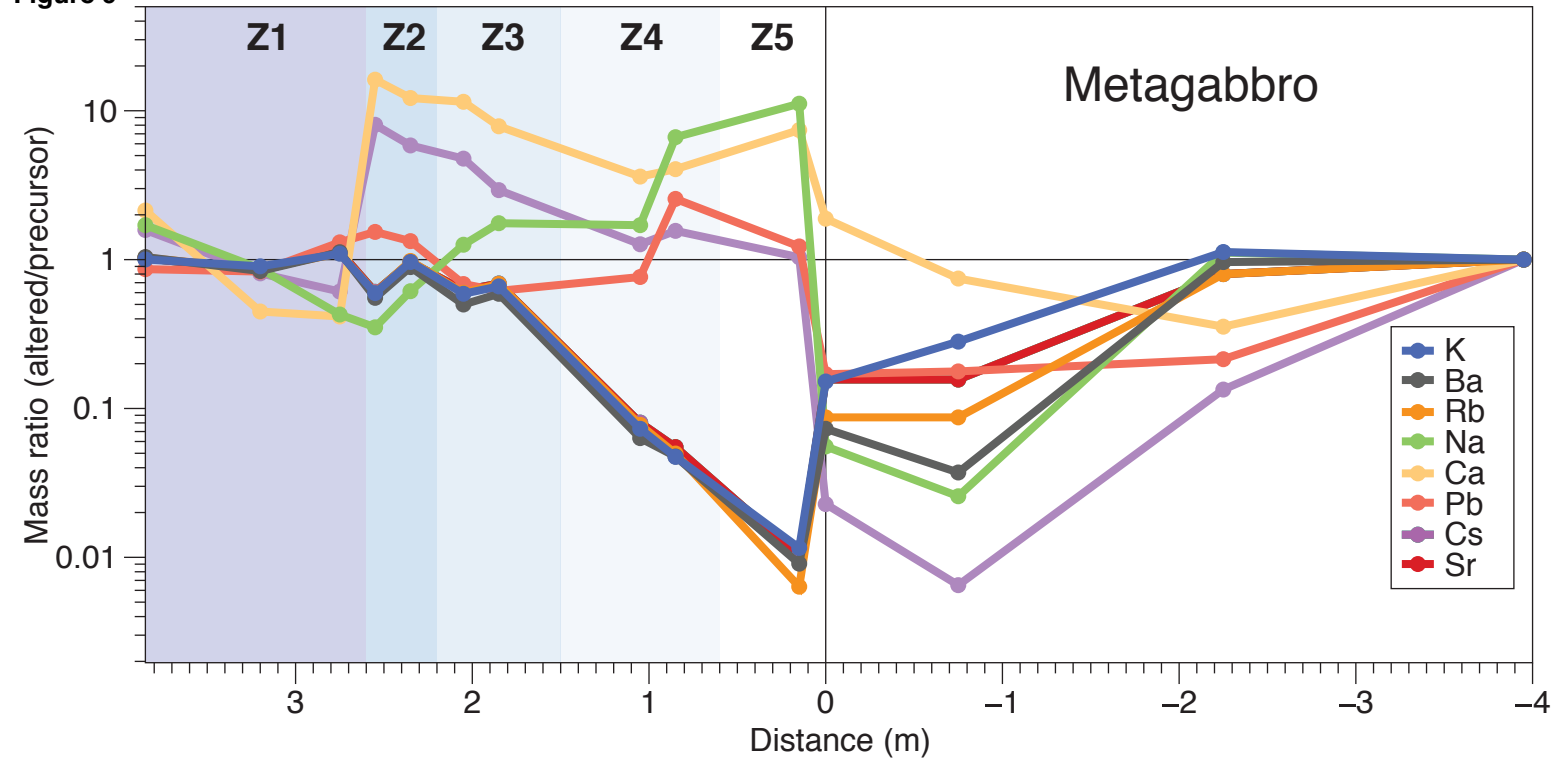


Figure 10

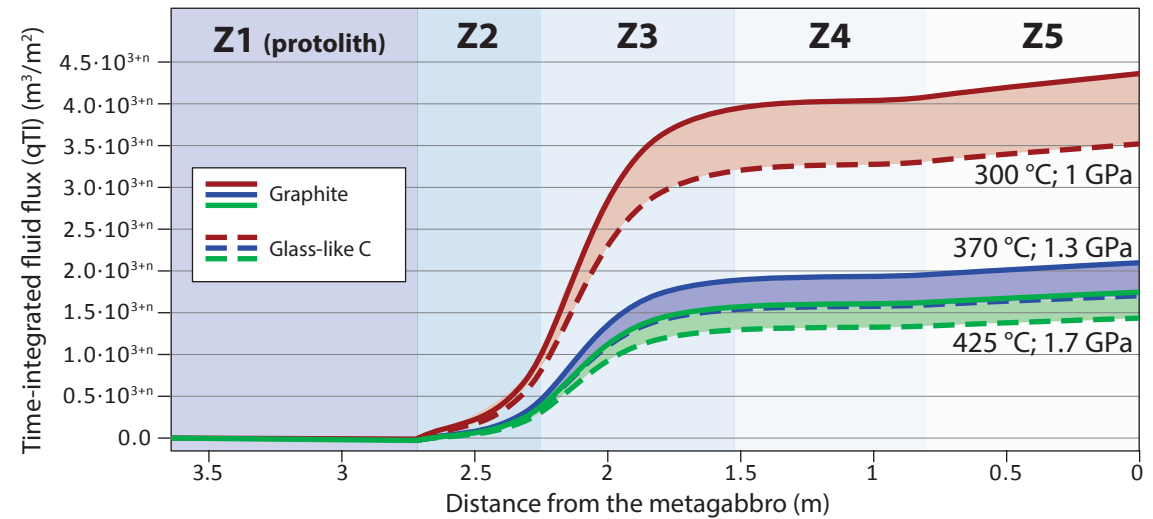


Figure 11

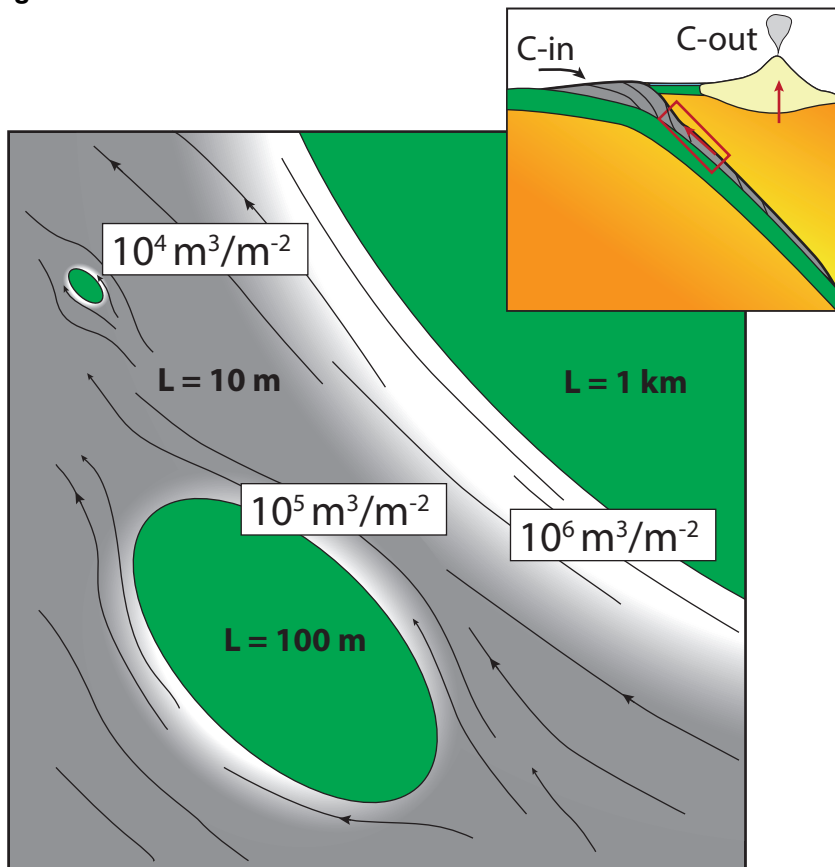


Table 1

Table 1. Bulk organic C and total CO₂ content in the selected samples across the metasomatic aureole.

Sample	Z1			Z2		Z3		Z4		Z5	Metagabbro			
	12-4	2h	2g	2f	2e	2d	2c	23	2b	24	25	28	2a	29
Corg (wt.%)	0.13	0.13	0.16	0.1	0.14	0.02	0.03	<DL	<DL	<DL	0.01	<DL	0.01	<DL
CO ₂ (wt.%)	0.63	0.68	0.68	0.93	0.63	0.24	0.13	0.06	0.06	0.04	0.09	0.09	0.08	0.02

Table 2

Table 2. RSCM R2 values of matrix and inclusion CM throughout the studied reaction zone.

Zone1		Zone2				Zone3				Zone4		Zone5
2G matrix		2G inclusion (Ttn)	2E matrix	2E inclusion (Law, Ttn)		2D matrix	2D inclusion (Law, Ttn)	2C matrix	2C inclusion (Law, Ttn)	23 matrix	23 inclusion (Law, Ttn)	24 inclusion (Ttn)
0.51	0.47	0.53	0.47	0.57	0.49	0.49	0.53	0.59	0.58	0.32	0.40	0.29
0.36	0.53	0.54	0.41	0.60	0.58	0.41	0.50	0.38	0.55	0.02	0.44	0.02
0.33	0.50	0.54	0.45	0.62	0.49	0.44	0.54	0.35	0.45	0.04	0.42	0.05
0.48	0.59	0.53	0.45	0.58	0.48	0.50	0.48	0.57	0.52	0.02	0.48	0.02
0.31	0.50	0.51	0.43	0.58	0.53	0.56	0.45	0.25	0.54	0.03	0.45	0.07
0.49	0.50	0.50	0.37	0.54	0.60	0.44	0.49	0.33	0.57	0.02	0.42	0.13
0.49	0.47	0.50	0.41	0.56	0.60	0.39	0.41	0.23	0.56	0.03		0.17
0.48	0.45	0.50	0.39	0.57	0.54	0.46	0.44	0.34	0.57	0.05		0.09
0.48	0.47	0.52	0.38	0.44		0.53	0.50	0.09	0.52	0.03		0.10
0.46	0.48	0.49	0.47	0.42		0.52	0.56	0.11	0.56	0.10		0.13
0.47	0.49	0.46	0.45	0.38		0.40	0.44	0.15	0.59	0.06		0.03
0.48	0.46	0.52	0.45	0.58		0.57	0.39	0.54		0.14		0.32
0.49	0.54	0.58	0.43	0.59		0.58	0.46	0.20		0.00		0.02
0.43	0.54		0.36	0.62		0.47	0.53	0.24		0.15		0.03
0.44	0.47		0.41	0.58		0.45	0.53	0.25		0.01		0.02
0.52	0.47		0.39	0.58		0.39	0.59	0.34		0.39		0.36
0.53	0.42		0.38	0.55		0.39	0.48	0.33		0.45		0.27
0.52	0.52		0.42	0.56		0.43	0.54			0.01		0.35
0.51	0.47		0.49	0.57		0.54	0.54			0.07		0.01
0.51	0.48		0.30	0.44		0.45	0.56			0.18		0.05
0.49	0.49		0.46	0.42		0.38	0.48			0.18		0.03
0.51	0.50		0.47	0.41		0.45	0.42					0.15
0.50	0.49		0.16	0.38		0.41	0.60					
0.52			0.50	0.58		0.49	0.49					
0.38			0.50	0.14		0.48	0.60					
0.07			0.48	0.58		0.46	0.60					
0.50			0.49	0.59		0.48						
0.45			0.33	0.58		0.55						
0.34				0.58		0.44						

Table 3

Table 3. Calculated fractional mass change and organic C loss per 100g of rock for Zr, Hf, and Th.

Sample	OC	Zr			Hf			Th		
		ppm	Fractional mass change (%)	Loss OC per 100g rock (g)	ppm	Fractional mass change (%)	Loss OC per 100g rock (g)	ppm	Fractional mass change (%)	Loss OC per 100g rock (g)
Zone1										
2g	0.160	122			3.4			13.04		
2h	0.130	108.3			3			10.09		
12-4	0.130	164			4.4			15		
Average	0.140	131.43			3.60			12.71		
SD	0.017	29.02			0.72			2.47		
Zone2										
2e	0.140	146	11	0.02	4.1	14	0.02	13.79	8	0.01
2f	0.100	105	-43	-0.06	2.9	-42	-0.06	10.7	-40	-0.06
Average	0.120	125.50	-16	-0.02	3.50	-14	-0.02	12.25	-16	-0.02
SD	0.028	28.99	38.20	0.05	0.85	40	0.06	2.18	34	0.05
Zone3										
2c	0.030	133	-78	-0.11	3.5	-79	-0.11	11.14	-81	-0.11
2d	0.020	102.2	-89	-0.12	2.8	-89	-0.12	9.887	-89	-0.12
Average	0.025	117.60	-84	-0.12	3.15	-84	-0.12	10.51	-85	-0.12
SD	0.007	21.78	7.48	0.01	0.49	7	0.01	0.89	5	0.01
Zone4										
2b	0.004*	239	-95	-0.13	5.9	-95	-0.13	4.639	-99	-0.14
23	0.004*	288.1	-94	-0.13	7.2	-94	-0.13	9.798	-98	-0.14
Average	0.004*	263.55	-94.27	-0.13	6.55	-95	-0.13	7.22	-98	-0.14
SD		34.72	0.75	0.00	0.92	1	0.00	3.65	1	0.00
Zone5										
24	0*	181.7	-100	-0.14	3.6	-100	-0.14	15.12	-100	-0.14

* <Detection limit (<0.01 wt.%); values calculated based on the proportions of disordered (R2>0.2) and graphitic (R2<0.2) CM.

Table 4. Fluid component speciation considered for mass balances and flux estimates, calculated by thermodynamic modelling of COH fluids saturated with graphite and glass-like carbon

	Buffer	P (GPa)	T (°C)	H ₂ O	CH ₄	CO ₂	X _C	molC/molH ₂ O
Graphite	H ₂ O max	1	300	0.99985	1.18E-04	3.55E-05	1.53E-04	1.53E-04
Glass-like C	H ₂ O max	1	300	0.99981	1.45E-04	4.37E-05	1.89E-04	1.89E-04
Graphite	H ₂ O max	1.3	370	0.99968	2.18E-04	9.99E-05	3.18E-04	3.18E-04
Glass-like C	H ₂ O max	1.3	370	0.99962	2.61E-04	1.20E-04	3.81E-04	3.82E-04
Graphite	H ₂ O max	1.7	425	0.99961	2.55E-04	1.33E-04	3.89E-04	3.89E-04
Glass-like C	H ₂ O max	1.7	425	0.99954	3.02E-04	1.58E-04	4.59E-04	4.59E-04

Table 5

Table 5. Calculated time-integrated fluid fluxes at H₂O-maximum. For each sample, qTI is calculated by considering the CM fractional change relative to the average of Z1.

Zone	Sample	L (m)	300 °C, 1.0 GPa		370 °C, 1.3 GPa		425 °C, 1.7 GPa		Zone	Sample	L (m)	300 °C, 1.0 GPa		370 °C, 1.3 GPa		425 °C, 1.7 GPa	
			qTI		qTI		qTI					qTI		qTI		qTI	
			Graphite	Glass-like C	Graphite	Glass-like C	Graphite	Glass-like C				Graphite	Glass-like C	Graphite	Glass-like C	Graphite	Glass-like C
Zone1	12-4	1	6.93E+02	5.63E+02	3.34E+02	2.78E+02	2.73E+02	2.31E+02	Zone3	2d	1	-3.86E+03	-3.13E+03	-1.86E+03	-1.55E+03	-1.52E+03	-1.29E+03
		10	6.93E+03	5.63E+03	3.34E+03	2.78E+03	2.73E+03	2.31E+03			10	-3.86E+04	-3.13E+04	-1.86E+04	-1.55E+04	-1.52E+04	-1.29E+04
		100	6.93E+04	5.63E+04	3.34E+04	2.78E+04	2.73E+04	2.31E+04			100	-3.86E+05	-3.13E+05	-1.86E+05	-1.55E+05	-1.52E+05	-1.29E+05
		1000	6.93E+05	5.63E+05	3.34E+05	2.78E+05	2.73E+05	2.31E+05			1000	-3.86E+06	-3.13E+06	-1.86E+06	-1.55E+06	-1.52E+06	-1.29E+06
	2h	1	-9.96E+02	-8.10E+02	-4.81E+02	-4.00E+02	-3.93E+02	-3.32E+02		2c	1	-3.38E+03	-2.75E+03	-1.63E+03	-1.36E+03	-1.33E+03	-1.13E+03
		10	-9.96E+03	-8.10E+03	-4.81E+03	-4.00E+03	-3.93E+03	-3.32E+03			10	-3.38E+04	-2.75E+04	-1.63E+04	-1.36E+04	-1.33E+04	-1.13E+04
		100	-9.96E+04	-8.10E+04	-4.81E+04	-4.00E+04	-3.93E+04	-3.32E+04			100	-3.38E+05	-2.75E+05	-1.63E+05	-1.36E+05	-1.33E+05	-1.13E+05
		1000	-9.96E+05	-8.10E+05	-4.81E+05	-4.00E+05	-3.93E+05	-3.32E+05			1000	-3.38E+06	-2.75E+06	-1.63E+06	-1.36E+06	-1.33E+06	-1.13E+06
	2g	1	1.25E+02	1.04E+02	2.60E+02	2.11E+02	1.02E+02	8.67E+01	Zone4	2b	1	-4.12E+03	-3.34E+03	-1.99E+03	-1.65E+03	-1.62E+03	-1.37E+03
		10	1.25E+03	1.04E+03	2.60E+03	2.11E+03	1.02E+03	8.67E+02			10	-4.12E+04	-3.34E+04	-1.99E+04	-1.65E+04	-1.62E+04	-1.37E+04
		100	1.25E+04	1.04E+04	2.60E+04	2.11E+04	1.02E+04	8.67E+03			100	-4.12E+05	-3.34E+05	-1.99E+05	-1.65E+05	-1.62E+05	-1.37E+05
		1000	1.25E+05	1.04E+05	2.60E+05	2.11E+05	1.02E+05	8.67E+04			1000	-4.12E+06	-3.34E+06	-1.99E+06	-1.65E+06	-1.62E+06	-1.37E+06
Zone2	2f	1	-1.86E+03	-1.51E+03	-8.99E+02	-7.48E+02	-7.34E+02	-6.21E+02		23	1	-4.07E+03	-3.31E+03	-1.96E+03	-1.64E+03	-1.60E+03	-1.36E+03
		10	-1.86E+04	-1.51E+04	-8.99E+03	-7.48E+03	-7.34E+03	-6.21E+03			10	-4.07E+04	-3.31E+04	-1.96E+04	-1.64E+04	-1.60E+04	-1.36E+04
		100	-1.86E+05	-1.51E+05	-8.99E+04	-7.48E+04	-7.34E+04	-6.21E+04			100	-4.07E+05	-3.31E+05	-1.96E+05	-1.64E+05	-1.60E+05	-1.36E+05
		1000	-1.86E+06	-1.51E+06	-8.99E+05	-7.48E+05	-7.34E+05	-6.21E+05			1000	-4.07E+06	-3.31E+06	-1.96E+06	-1.64E+06	-1.60E+06	-1.36E+06
	2e	1	4.77E+02	3.87E+02	2.30E+02	1.91E+02	1.88E+02	1.59E+02	Zone5	24	1	-4.33E+03	-3.52E+03	-2.09E+03	-1.74E+03	-1.71E+03	-1.45E+03
		10	4.77E+03	3.87E+03	2.30E+03	1.91E+03	1.88E+03	1.59E+03			10	-4.33E+04	-3.52E+04	-2.09E+04	-1.74E+04	-1.71E+04	-1.45E+04
		100	4.77E+04	3.87E+04	2.30E+04	1.91E+04	1.88E+04	1.59E+04			100	-4.33E+05	-3.52E+05	-2.09E+05	-1.74E+05	-1.71E+05	-1.45E+05
		1000	4.77E+05	3.87E+05	2.30E+05	1.91E+05	1.88E+05	1.59E+05			1000	-4.33E+06	-3.52E+06	-2.09E+06	-1.74E+06	-1.71E+06	-1.45E+06